UNIVERSITY OF VERONA

PhD Course in Cardio-vascular Sciences

XXXV° CYCLE

An Image-Based Computational Fluid Dynamics Study of Mitral Valve.
A novel Approach to Assess the Mitral Valve, from Physiology to Surgical Practice

Program Director

Prof. ANDREA RUZZENENTE

Tutor

Prof. GIOVANNI BATTISTA LUCIANI

PhD Student

VINCENZO GIAMBRUNO

Index

Abstract

Mitral valve disease is the second most frequent valve disease requiring surgery. The aim of our study was to develop through a computational fluid dynamics a method to study the mitral valve from Pathophysiology to mitral valve regurgitation undergone surgical repair.

As a first stage, we performed computational fluid dynamic (CFD) simulations in the left ventricle, left atrium and aortic root, with a resistive immersed method, a turbulence model, and with imposed systolic wall motion reconstructed from Cine-Magnetic Resonance Imaging (MRI) images, which allowed us to segment also the mitral valve. For the regurgitant scenarios we considered an increase of the heart rate and a dilation of the left ventricle.

Our results highlighted that mitral varve regurgitation (MVR) gave rise to regurgitant jets through the mitral orifice impinging against the atrial walls and scratching against the mitral valve leading to high values of wall shear stresses (WSSs) with respect to the healthy case.

CFD with prescribed wall motion and immersed mitral valve revealed to be an effective tool to quantitatively describe hemodynamics in case of MVR and to compare different regurgitant scenarios. Our findings highlighted in particular the presence of transition to turbulence in the atrium and allowed us to quantify some important cardiac indices such as cardiac output and WSS.

After validation of the model, we performed a computational image-based study of blood dynamics in the whole left heart, both in a healthy subject and in a patient with MVR. We elaborated dynamic cine-MRI images with the aim of reconstructing the geometry and the corresponding motion of left ventricle, left atrium, mitral and aortic valves, and aortic root of the subjects. This allowed us to prescribe such motion to computational blood dynamics simulations where, for the first time, the whole left heart motion of the subject is considered, allowing us to obtain reliable subject-specific information. The final aim was to investigate and compare between the subjects the occurrence of turbulence and the risk of hemolysis and of thrombi formation. In particular, we modeled blood with the Navier-Stokes equations in the Arbitrary Lagrangian-Eulerian framework, with a Large Eddy Simulation model to describe the

transition to turbulence and a resistive method to manage the valve dynamics, and we used a Finite Elements discretization implemented in an in-house code for the numerical solution. Our results highlighted that the regurgitant jet in the MVR case gave rise to a large amount of transition to turbulence in the left atrium resulting in a higher risk of formation of hemolysis. Moreover, MVR promoted a more complete washout of stagnant flows in the left atrium during the systolic phase and in the left ventricle apex during diastole.

This work put the base for a new clinical approach to the mitral valve such as the analysis and the comparison of different surgical techniques of the diseased mitral valve undergone a surgical repair.

1. An Image-Based Computational Fluid Dynamics Study of Mitral Regurgitation in Presence of Prolapse, Construction and validation of a model

1.1 Introduction

Mitral valve regurgitation (MVR) is a congenital or acquired pathological condition of the mitral valve leading to an incomplete closure of the leaflets during the systolic phase, causing a retrograde blood flow from the left ventricle to the left atrium. The major complications are atrial fibrillation or flutter, pulmonary arterial hypertension and heart failure [69]. Epidemiological studies estimated that MVR occurs in up to 10% of the worldwide population [41]. The quantitative assessment of blood dynamics quantities, such as pressure, velocity and stresses, in presence of MVR during the systolic phase is crucial for the understanding of the phenomena and to elaborate the diagnosis. For example, the regurgitant volume (RV) and the regurgitant fraction (RF) can help physicians in assessing the severity of the pathological condition [73] and potentially helping the design of treatments [33, 54]. Computational methods in realistic cardiac geometries represent a non invasive way to provide blood dynamics information [26] and help the surgeons, e.g., by suggesting possible clinical indications for the surgical treatment of the systolic anterior motion [29] and of septal myectomy for hypertrophic obstructive cardiomyopathy [84]. Computational studies investigating the mitral valve and its interaction with the blood flow have been proposed since the early 2000s, and can be divided into two categories: (i) fluid–structure interaction (FSI) models and (ii) computational fluid dynamics (CFD) models with imposed wall motion. Regarding the FSI approach, some authors investigated the mitral valve dynamics in physiological conditions [76, 3, 44, 40, 28, 48, 77], in case of calcific leaflets [40], to model surgical interventions as the neochordae replacement [27], and to account for MVR [35, 74]. In Ref. [74], MVR has been modeled by means of an idealized diode whilst in Ref. [35] the healthy configuration has been deformed. The majority of these works [76, 3, 44, 40, 28, 48] used the immersed boundary method (IBM), proposed in Refs. [48, 5]. In order to reduce the high computational costs of FSI

simulations, CFD models with imposed ventricular and leaflets motion provided by dynamic imaging have also been considered. Such models require a great effort in elaborating the dynamic images and in merging them with CFD. However, they noticeably simplify the problem from the modeling point of view. The majority of such works are based on images provided by ultrasound (US) techniques (like 3D echocardiography). 3D Echo has the advantage of providing high temporal resolution, particularly useful when resolving the rapid movements of the mitral valve leaflets [84]. For example, in Refs. [55, 47] the authors prescribed both the ventricle and the mitral valve motion to study the ventricular flow in physiological
conditions. In Ref. [53], the authors reconstructed the ventricle size and shape from computer tomography (CT) scans and the mitral valve from US to predict the outcomes of the mitraclip, a surgical technique used to restore the mitral valve function. Another dynamic imaging technique used for ventricular CFD is Cine-MRI. However, such technique has been used to reconstruct only the motion of the ventricle whereas different models of the mitral valve have been considered. For example, we cite Ref. [18] where the authors investigated the effect of incorporating an idealized mitral valve in patients affected by pulmonary artery hypertension, and
Refs. [29, 88] where a template of mitral valve was included to study the systolic anterior motion and the hypertrophic cardiomyopathy. Regarding the study of the MVR by CFD with imposed motion, we cite Refs. [10, 16], where the authors tested and compared different types of mitral valve prolapse from US images and different degrees of MVR from CT images. This work aims at providing an original study of the systolic blood dynamics in the left ventricle in physiological and MVR conditions. For this purpose, we introduced some contributions in the context of computational models for ventricular fluid-dynamics. First, we adapted to the systolic phase (closed mitral valve) a method based on radial sampling Cine-MRI acquisitions developed in Ref. [67] for the diastolic phase and applied to a structural analysis. Second, we applied, for the first time, such reconstruction, from radial sampling Cine-MRI, to the context of a systolic CFD with ventricular motion, obtained by a (not radial) Cine-MRI acquisition. The third contribution of this work consisted in the comparison of the systolic blood dynamics in physiological and MVR conditions, where for the latter

case we considered two scenarios, i.e. an increment of the heart rate and a ventricular dilation [60].

1.2 Materials and Methods

1.2.1 Description of the Scenarios

In this work we provided a comparison of blood flow dynamics in scenarios with healthy and regurgitant mitral valves during the systolic phase. To do this, we considered the same geometric and moving conditions for the left ventricle, for the aorta, and for the left atrium. In this respect, we created three different virtual scenarios:

- *healthy* (H): we inserted a structurally normal mitral valve (taken from dedicated MRI images) and we considered a heart rate equal to 75 bpm/min (duration of the systolic phase T_S = 0.32 s);
- *regurgitant with increased heart rate* (R1): we inserted a regurgitant mitral valve with a posterior leaflet prolapse of the P2 segment (reconstructed from dedicated MRI images) and we increased the basal heart rate to 90 bpm/ min (T_S = 0.26 s [32, 62]);
- *regurgitant with dilatation* (R2): we inserted the same regurgitant mitral valve of R1, with heart rate equal to 75 bpm/min, and we dilated all the geometry (ventricle, atrium, aorta).

The regurgitant scenarios represent different stages of the pathological evolution of the heart function in case of MVR due to prolapse, leading to a decrease of the cardiac output (CO). To compensate, in an *early stage* the heart rate spontaneously increases (R1) [60]. However, this leads to a reduction of the duration of the diastolic phase, making the coronary arteries perfusion less effective over the time. Thus, in a *medium-long term*, the early compensatory changes are gradually replaced by a remodeling process with dilation of the left ventricle and restoring of the basal heart rate (R2). The resultant increase of the stroke volume (SV) tends to compensate for the low CO [60].

1.2.2 Acquisition of Cine-MRI Image

Cardiac Cine-MRI data were provided by the Department of University Hospital of Verona, Italy. Ethical Review Board approval and informed consent were obtained from all patients.

The acquisitions were performed with the Achieva 1.5T (TX)-DS (Philips, Amsterdam, Netherlands) technology with the following characteristics:

- *Left ventricle*: (i) volumetric short-axis series made of 15 slices with thickness and distancing of 8 mm along the left ventricle main axis, with a spatial resolution of 1 mm; (ii) a set of single-slices, two-dimensional long- axis acquisitions on the so-called two-chamber and four- chamber planes, with space resolution of 1 mm and slice thickness of 8 mm. Both series had a time resolution equal to 30 frames/cardiac cycle. This protocol was carried out for a subject who did not present any alteration of the left ventricle wall and movement;
- *Mitral valves*: two-dimensional long-axis series of 18 evenly rotated (one every 10) planes around the axis passing through the annular center and aligned with the left ventricle. Time resolution equals to 30 frames/cardiac cycle, spatial resolution equals to 1.25 mm, and slice thickness to 8 mm. This protocol was repeated for both a healthy patient and one with a regurgitant mitral valve.

In what follows we describe how such images were elaborated and reconstructed.

1.2.3 Geometric Reconstruction of the Left Ventricular Endocardium

In this section we describe the strategy followed to reconstruct the geometry and the displacement field of the left ventricular endocardium.

The starting point were the volumetric short-axis images, which are *ad hoc* series for the reconstruction of the left ventricular anatomy. However, one of the main disadvantages often characterizing such images in the daily clinical practice is the low resolution among slices (in our case about 8 mm). As a consequence, it is difficult to capture some important findings of the heart contraction, as the longitudinal shortening of the ventricle. To account for this, in this work we applied the short–long axis merging (SLAM) algorithm, proposed in Refs. [88, 31], which consists in enhancing

the short-axis images by merging them with long-axis acquisitions (2 and 4 chambers views). For each available time instant, this procedure requires three main steps:

(1) creation of a new artificial image with the same dimensions of the short-axis view and with a uniform space resolution (1 mm in our case) in all three Cartesian directions;

(2) for each voxel V of this new artificial image, identify, for each slice of the original Cine-MRI image, the nearest voxel, and compute the distance d^V between the two;

(3) compute the weighted average of the values of the voxels identified at point 2, where the weights depend on d^V, and assign it as a gray level of V.

These steps lead to an enhanced time-dependent series of volumetric images with a uniform space resolution of 1 mm in all directions, including the cross-slice one.
Starting from these enhanced images, we segmented and reconstructed the shape of the endocardium and epicardium at six instants from the end diastolic (ED) to the end systolic (ES) configuration, by adopting the semi-manual segmentation algorithm proposed in Ref. [7] and implemented in the Medical Image Toolkit (MITK) open-source software (www.mitk.org) [11, 22]. This algorithm is based on a manual identification of the endocardial and epicardial 2D contours on each slice. Then, a smooth 3D surface is created by a 3D radial basis function interpolation of the 2D contours, based on the intensity of the image.

After, we performed a Boolean difference between the epicardium and the endocardium, in order to extract the region of the endocardium from the apex to the level of the valvular ring by using the Vascular Modeling Toolkit (VMTK) (www.vmtk.org) [46] and suitable tools for cardiac mesh generation [61]. We point out that during the identification of the ventricular endocardial contour, we included also the area occupied by the papillary muscles, in order to obtain a regular surface. This is a common choice adopted also in Refs. [29, 88, 78].

These steps were repeated for all the six frames, obtaining surface meshes made of triangles, representing the configurations of the endocardium during its contraction phase. Then, we registered the displacement needed to pass from a configuration to another one by exploiting the non-affine B-splines algorithm implemented in the

Elastix open source library (http://elastix.isi.uu.nl), consisting in the minimization of the difference between two images under the assumption that they represent the same region, i.e. the same bounding box [86]. In particular, in our work, chosen a reference configuration, this was deformed to recover all the other frames. Calibration of registration parameters was performed in order to avoid possible formation of skewed triangles. The registration was run in serial on a Linux working station. This allowed us to compute the displacement fields (with respect to the ES configuration) at the six different time instants.

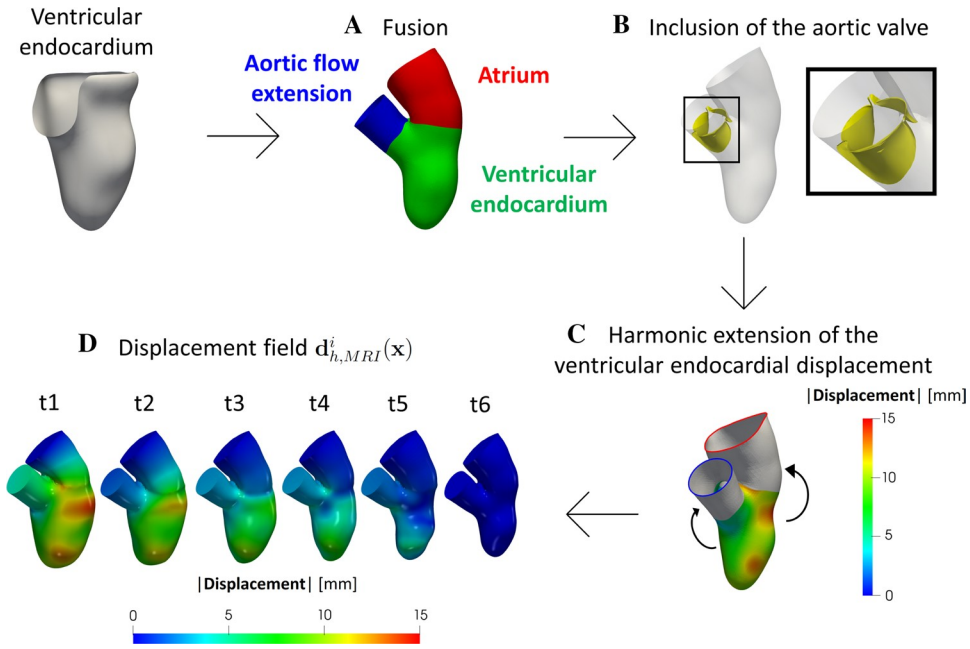

Fig. 1 Steps to complete the geometry and its displacement. (A) Union of the atrium with the ventricular endocardium and addition of an aortic flow extension. (B) Inclusion of a template of the aortic valve (as an example, here we reported the open configuration). (C) Harmonic extension of the ventricular endocardial displacement for the atrium and for the aorta. (D) Geometries of the six current configurations together with the corresponding magnitude of the displacement field $\mathbf{d}^i_{h,MRI}(\mathbf{x})$ with respect to the ES instant

1.2.4 Inclusion of Left Atrium, Aortic Valve, and Aorta

We completed the ventricular geometry by adding left atrium, aortic root and aortic valve. The strategy adopted is showed in Fig. 1. Since the ventricular Cine-MRI images at disposal were not sufficient to allow a 3D reconstruction of the left atrium, aorta and aortic valve, that are only partially visible in long-axis images, we considered a template geometry of the internal atrial surface and the aortic valve from the *Zygote solid 3D heart model*, a complete geometry reconstructed from CT scans representing an average healthy heart (https://www.zygote.com). In particular, we merged such templates to the ES configuration of the reconstructed ventricular endocardium. For the healthy case H, we started our simulation at the aortic valve opening instant t_0 since we could not simulate the isovolumic phases. Indeed, the pressure, when both the valves are closed, is not uniquely defined due to the absence of a stress condition on a part of the fluid boundary domain (like, instead, happens at the atrial outflow in the regurgitant cases) [38, 17]. For the regurgitant cases, instead, general clinical observations show that MVR lowers the ventricular pressure until to be smaller than the aortic one, delaying the aortic valve opening. Thus, in R1 and R2, both valves are in their closed configuration at the initial time t_0 in order to prevent an inward flow from the aorta to the left ventricle at the beginning of systole. In this case, owing to the systolic stress condition at the mitral orifice due to the atrial pressure, we are able to start the simulation from the configuration where both valves are closed. Moreover, we generated an aortic flow extension of the left ventricle outflow tract to account for the aorta (steps A and B in Fig. 1). These operations were done by using suitable algorithms in VMTK which, in particular, allowed us to connect harmonically two surfaces (*vmtksurfaceharmonicconnector*), to project a displacement field on a surface (*vmtksurfaceprojection),* and to solve harmonic extension problem (*vmtksurfaceharmonicextension)* [61). This allowed us to obtain a surface mesh of the complete geometry (ventricular endocardium, left atrium and aorta) at the ES configuration. Then, to provide a displacement field also to the atrium and the aortic root, we harmonically extended the ventricular endocardial displacement to the corresponding surfaces (step C in Fig. 1). The reason why we selected an harmonic extension was due to the smooth solution provided by this operator, thus guaranteeing an homogeneous overall displacement. In such a way, a displacement field was

defined for each point of the complete mesh at each of the six frames. After, we performed a L^2 projection of such data on the computational mesh used to perform Finite Elements simulations (see next section) to obtain the functions $\mathbf{d}^i{}_{h,MRI}(\mathbf{x})$, $i = 1, \dots, 6$ [see step D in Fig. 1 where we reported the six configurations obtained together with the magnitude of $\mathbf{d}^i{}_{h,MRI}(\mathbf{x})$,]. Notice that the first instant (t1) refers to the ED configuration, whereas the last one (t6) to the ES configuration.

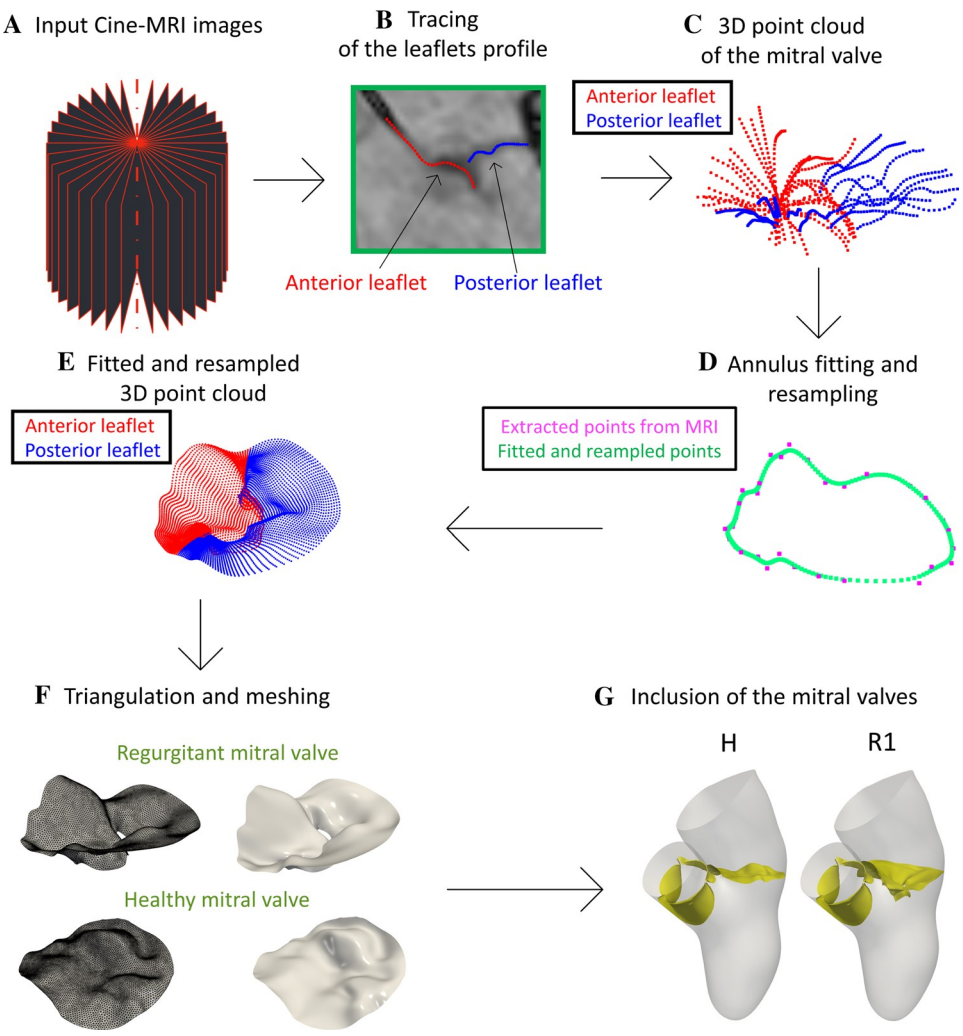

Fig. 2 Flow chart to reconstruct the mitral valves and to define the virtual scenarios.(A) Cine-MRI images of the mitral valve. (B) Tracing of the leaflets profile on each of the 18 longitudinal planes. (C) 3D point cloud of the mitral valve obtained by tracing the leaflets profiles in all the planes. (D) Fitting and resampling procedure of the rings (the case of the annulus is reported here as an example). (E) The 3D point cloud as a result of the fitting and resampling procedure performed for all the rings. (F) Creation of a surface mesh of the mitral valve. (G) Generation of scenarios H and R1 (to obtain scenario R2, we dilated the geometry and the displacement field of R1 by a factor 1.25)

1.2.5 Geometric Reconstruction of the Mitral Valve

In this section we reported the steps followed to reconstruct the two mitral valves at disposal in the systolic configuration and to build the three virtual scenarios under study (see "Description of the Scenarios" section). For the reconstruction of the mitral valves, we adapted to the systolic phase the method proposed in Ref. [67] for the diastolic case, see Fig. 2. The starting point are Cine-MRI images of a healthy and of a regurgitant mitral valve acquired based on a protocol proposed for the first time in Ref. [67]. The operator performed a radial sampling by using 18 planes rotated every 10 around the axis passing through the center of the annular plane and aligned with the left ventricle apex. The result of this protocol is reported in step A in Fig. 2 and represents the input data to reconstruct the mitral valve. Then, such mitral images were imported in 3D Slicer (https://slicer.org/) and for each of the 18 acquired longitudinal planes we traced the leaflets profile in the ED configuration by using a spline curve sampled in 32 points (step B in Fig. 2). In the healthy case, in order to guarantee a full closure, we imposed that the positions of last points of the anterior and posterior leaflet profiles were equal. We repeated this operation for all the 18 planes to obtain the final 3D point cloud representing the mitral valve profile (step C in Fig. 2). These data are stored in a matrix of cloud points composed by 1152 rows (32 sampling points 36 leaflets profiles) 3 columns (x, y and z coordinate). After, we imported this matrix in MATLAB (www.mathworks.com) to perform a smoothing process in order to reduce possible inaccuracies due to image noise and to the manual segmentation of the leaflets. To do this, we created a new matrix where blocks of 36 consecutive rows represent the (36) points of a ring (32 rings in total), with the first ring corresponding to the annulus and the last one to the free margin. Then, the points of each ring were fitted by using a B-Spline (see step D in Fig. 2). This resulted in a new 3D point cloud of 32,000 rows (1000 points 32 rings) 3 columns (x, y and z coordinate), see step E in Fig. 2. After, for each of the 3D point cloud of two mitral valves, a preliminary surface mesh was generated in MATLAB and then remeshed with a uniform edge length using MeshMixer (https://www.meshmixer.com), see step F in Fig. 2. Finally, the mitral valves were added to the reconstructed geometry (Fig. 1) to build the three virtual scenarios under study (step G in Fig. 2). In particular, to guarantee a perfect adhesion between the mitral

annulus and the ventricle, we placed the mitral valve in the valvular plane of the reconstructed geometry at the ES instant (see Fig. 1, step D) and calculated the minimum distance of the annulus with respect to the wall. After, we harmonically extended this distance over all the mitral valve by using the same harmonic extension algorithm used to extend the ventricular endocardial displacement. Finally, we warped the mitral valve according to such displacement (for the aortic valve we adopted the same strategy). We point out that geometry and displacement field $\mathbf{d}^{i}{}_{h,\,MRI}(\mathbf{x})$ of H and R1 are the same at each of the six time instants (see Fig. 1, step D). Instead, to obtain the configuration of R2, in absence of patient-specific data, we dilated the geometry of R1 to reach a diameter of the left ventricle cavity equal to 7.2 cm; this represents a characteristic value of the maximum diameter of a dilated left ventricle cavity in presence of MVR according to [40, 41]. To do this, we expanded at each time frame the R1 geometry and the displacement field $\mathbf{d}^{i}{}_{h,\,MRI}(\mathbf{x})$ by a factor of 1.25. We employed the same dilation factor (1.25) for the whole geometry because of the difficulty to predict left atrium and aorta dilation. Indeed, they are dependent upon several variables, including, but not limited, to the degree and duration of MVR, the presence of associated lesions of the aortic valve and/or the ascending aorta, the presence and type of acute or chronic arrhythmias, the left ventricular function, the presence and degree of systemic hypertension, the utilization of medications to reduce pressure and/or volume overload [42–45].

In Figure 3, we showed a section of the regurgitant mitral valve (starting from the surface obtained at Step F above in Fig. 2). In red we reported the anterior leaflet and in blue the posterior one. As said, this valve has a posterior leaflet prolapse of the P2 segment, namely a displacement of the leaflet towards the left atrium [46]. The prolapse is emphasized by comparing the real pathological (prolapsed) posterior leaflet (B, in blue) with a possible configuration of the posterior leaflet in the healthy configuration (A, dashed line).

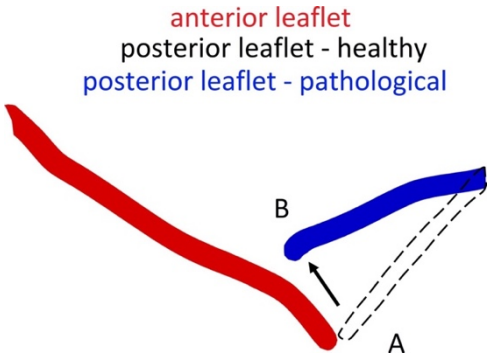

Fig. 3 Section of the mitral valve with prolapse of the posterior leaflet. In red the anterior leaflet and in blue the posterior one. The dashed curve represents a possible position of the posterior leaflet in the healthy configuration. The prolapse of the P2 segment moves the posterior leaflet from configuration A to B towards the atrium.

1.2.6 Mathematical and numerical modeling

Let $\Omega(t)$ be the computational moving domain of the complete geometry. The boundaries of $\Omega(t)$ are displayed in Figure 4, left. The motion of Ω is determined by the displacement field $\mathbf{d}^i_{\text{h,MRI}}(\text{X})$ reconstructed and showed in Fig. 1. However $\mathbf{d}^i_{\text{h,MRI}}(\mathbf{X})$ has been obtained only at the MRI acquisition times ($i = 1, \ldots, 6$) and thus we employed a spline interpolation to obtain $\mathbf{d}_{h,MRI}(\mathbf{x}, t)$ for all $t \in [0, T_S]$.

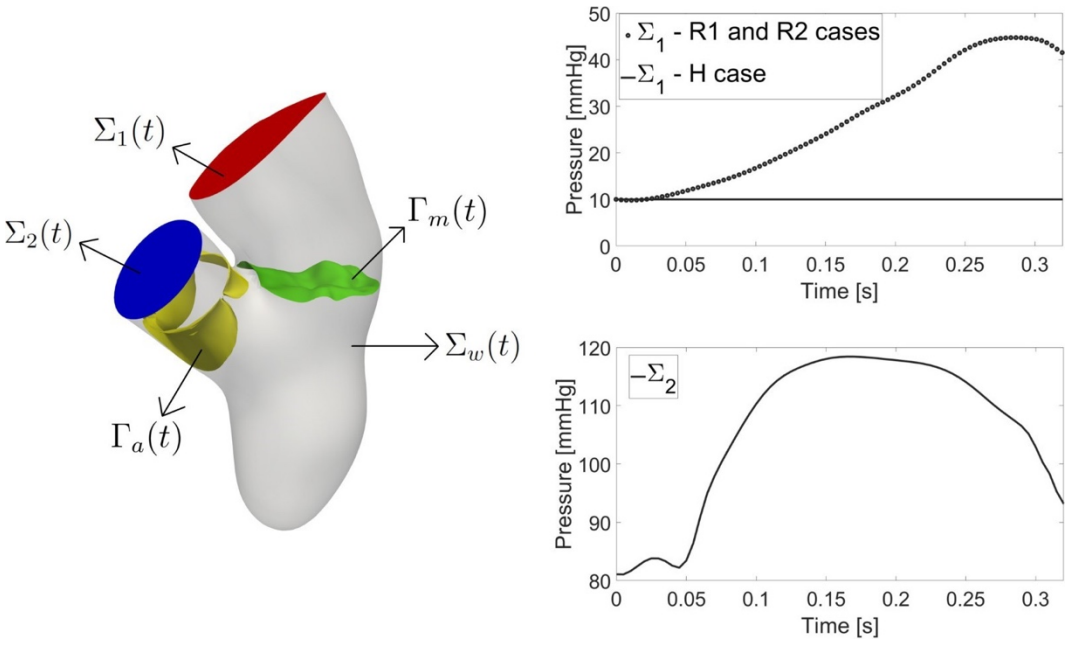

Fig. 4 Left: computational domain $\Omega(t)$ with its boundaries: Σw (t) represents the ventricular endocardium and the physical wall of the atrium and aortic root; $\Sigma_1(t)$ is the atrium outlet (in red) and $\Sigma_2(t)$ the aortic outlet (in blue). $\Gamma_a(t)$ is the surface of the aortic valve and $\Gamma_m(t)$ the surface of the mitral valve. Right: trend in time of the pressure imposed at the outlets $\Sigma_1(t)$ (up) and $\Sigma_2(t)$ (bottom) (for R1 the frequency has been suitably adapted).

We considered blood as an incompressible Newtonian fluid with density $\rho = 1.06\ 10^3$ kg/m^3 and dynamic viscosity $\mu = 3.5\ 10^{-3}$ $Pa\ s$. The systolic contraction of the complete geometry is taken into account by solving the fluid problem in an Arbitrary Lagrangian–Eulerian (ALE) formulation [47, 48]. The fluid domain is obtained by starting from the ventricular displacement $\mathbf{d}_{h,MRI}$ and by extending it into $\boldsymbol{\Omega}$ through the solution of a linear elastic problem [49]. The presence of the valves is accounted by a resistive immersed method inspired by the one proposed in [50, 51]. In particular, we used the Resistive Immersed Implicit Surface (RIIS) method, whose main advantage is that the computational mesh and the surface of the valve do not need to be conforming [52]. Specifically, the RIIS method introduces, into the momentum balance of the Navier-Stokes equations, an additional term which penalizes the kinematic condition representing the adherence of the blood to the valves. To capture the transition to turbulence [53], we used the Large Eddy Simulation (LES) σ-model proposed for ventricular blood dynamics in [54] and successfully used in different hemodynamic applications [55–57]. In particular, this turbulence model is suited to handle wall bounded flows in complex geometries, such as ventricle and atrium [54]. In this framework, let index n indicate the approximation of quantities at time $t^n = n\ t$, where Δt is the time discretization parameter. Then, with a first-order semi-implicit time discretization, the problem at time step t^{n+1} reads:

1) Solve a linear elasticity problem to find the displacement $\mathbf{d}^{n+1}$ of the fluid domain[3]:

$$\begin{cases} -\nabla \cdot \left[2\mu_{\mathrm{EXT}} \nabla^s \hat{\mathbf{d}}^{n+1} + \lambda_{\mathrm{EXT}} \left(\nabla \cdot \hat{\mathbf{d}}^{n+1} \right) \mathbf{I} \right] = \mathbf{0} & \text{in } \hat{\Omega}, \\ \hat{\mathbf{d}}^{n+1} = \hat{\mathbf{d}}^{n+1}_{\mathrm{h,MRI}} & \text{on } \hat{\Sigma}_w, \\ \hat{\mathbf{d}}^{n+1} = \mathbf{0} & \text{on } \hat{\Sigma}_1, \\ \left[2\mu_{\mathrm{EXT}} \nabla^s \hat{\mathbf{d}}^{n+1} + \lambda_{\mathrm{EXT}} \left(\nabla \cdot \hat{\mathbf{d}}^{n+1} \right) \mathbf{I} \right] \cdot \hat{\mathbf{n}} = \mathbf{0} & \text{on } \hat{\Sigma}_2, \end{cases} \tag{1}$$

with the symmetric gradient and $\mathbf{I}$ the identity matrix. μ_{EXT} and λ_{EXT} were both set to be the value of 0.4 Pa to avoid mesh elements degeneration during the deformation.

Notice the homogeneous Dirichlet condition on Σ_1, since we want to keep fixed the atrial section, and the homogeneous Neumann condition on Σ_2 in order to let it free to move in accordance with the rest of the geometry.

2) Update the fluid domain $\Omega^{n+1}= \Omega\hat{} + \mathbf{d}\hat{}^{n+1}$ and calculate the fluid domain velocity $\mathbf{u}\hat{}^{n+1}_{ALE} = (\mathbf{d}\hat{}^{n+1}-\mathbf{d}\hat{}^{n})/\Delta t$;
3) Compute the wall velocity $\mathbf{u}\hat{}^{n+1}_{h,MRI}=(\mathbf{u}\hat{}^{n+1}_{h,MRI} - \mathbf{u}\hat{}^{n+1}_{h,MRI})/\Delta t$;

4) Solve the ALE Navier–Stokes equations in the known domain Ω^{n+1} to find the pressure p^{n+1} and the blood velocity $\mathbf{u}^{n+1}$:

$$\begin{cases} \rho\dfrac{\mathbf{u}^{n+1}-\mathbf{u}^{n}}{\Delta t} + \rho\left(\mathbf{u}^{n}-\mathbf{u}^{n+1}_{\mathrm{ALE}}\right)\cdot\nabla\mathbf{u}^{n+1} \\ \quad -\nabla\cdot\left(2(\mu_{\mathrm{sgs}}(\mathbf{u}^{n})+\mu)\mathbf{D}(\mathbf{u}^{n+1})\right) + \nabla p^{n+1} \\ \quad +\sum_{i=a,m}\dfrac{R}{\varepsilon}\left(\mathbf{u}^{n+1}-\mathbf{u}^{n+1}_{\Gamma_i}\right)\delta_{\Gamma_i,\varepsilon_i} = \mathbf{0} \qquad \text{in } \Omega^{n+1}, \\ \nabla\cdot\mathbf{u}^{n+1} = 0 \qquad \text{in } \Omega^{n+1}, \\ \mathbf{u}^{n+1} = \hat{\mathbf{u}}^{n+1}_{\mathrm{h,MRI}} \qquad \text{on } \Sigma_{\mathrm{w}}^{n+1}, \end{cases} \tag{2}$$

with a null initial condition in Ω^0.

The convective term in the momentum equation is treated in a semi-implicit way. The velocity strain rate tensor $\mathbf{D}(\mathbf{u}^{n+1})$ is defined by $\mathbf{D}(\mathbf{v})=(\nabla\mathbf{v}+(\nabla\mathbf{v})^{T})/2$. The sub-grid viscosity μ_{sgs} of the σ-model is given by

$\mu_{sgs}=\rho C\Delta^2\sigma_3(\sigma_1-\sigma_2)(\sigma_2-\sigma_3)/\sigma^2_1$ with $\sigma_1(\mathbf{x})>\sigma_2(\mathbf{x})>\sigma_3$ the singular values of $\nabla\mathbf{u}^n$. The average mesh element size Δ is equal to 1.5 mm for scenario H and R1 and 1.9 mm for R2 while C is a constant set to the value of 1.5 [42, 2]. Notice the explicit treatment of the LES non-linearity.

In the RIIS model, R is the resistance coefficient, whereas ε is half of the leaflets thickness. For both the mitral and aortic valves, we set $R=10^4$ kg/m s, a penalization large value used to enforce the kinematic constraint [29], and ε=0.75 mm. The prescribed leaflets velocity $\mathbf{u}^{n+1}_{1\Gamma i}$, $i=m,a$, is zero for the mitral valve, since we

considered only the closed configuration, and for the aortic valve, since the opening/closure mechanism (occurring only in the regurgitant cases R1 and R2) was modeled in an on/off modality, by considering the two geometric configurations (open/closed) of the aortic valve template. The opening phase (modeled for R1 and R2, see "Inclusion of Left Atrium, Aortic Valve, and Aorta" section) was instantaneous and triggered by a positive pressure jump between the ventricle and the aorta, whereas the closure occurred when a negative flow rate developed at the aortic valve plane [36, 55]. Furthermore, in order to guarantee a perfect adhesion between the valves and the walls at each time instant, we imposed both the valves to move in accordance with the ALE displacement.

Finally, we have that $\delta_{\Gamma i,\varepsilon i}$,i=m,a, is a smoothed Dirac delta function representing a layer, with thickness 2ε, around the surface of the valve, given by the following expression [21, 29]:

$$\delta_{\Gamma_i,\varepsilon_i}(\varphi_i) = \begin{cases} \dfrac{1+\cos(\pi\varphi_i/\varepsilon_i)}{2\varepsilon_i} & \text{if} \quad |\varphi_i| \le \varepsilon_i, \\ 0 & \text{if} \quad |\varphi_i| > \varepsilon_i, \end{cases} \tag{3}$$

where φ_i is a signed distance function that implicitly describes the ith immersed surface Γ_i as $\Gamma_i = \{\mathbf{x} : \varphi_i(\mathbf{x}) = 0\}$.

Regarding the boundary conditions for problem (2), at the atrial outlet Σ_1, we prescribed a constant pressure of 10 mmHg taken from the Wiggers diagram [58] for scenario H, and a time dependent pressure taken from Refs. [35, 75] for the regurgitant scenarios R1 and R2 (Fig. 4, right). In the latter cases, the authors observed that the formation of a RV in the atrium results in a marked increase of the atrial pressure (elevated V-wave). Nevertheless, in absence of any information about the range of validity of the pressure waveform provided in Refs. [35, 75], we applied it to both R1 and R2 cases. In addition, in scenarios R1 and R2, to avoid possible backflows instabilities, we imposed null tangential velocity [50]. At the aorta outlet Σ_2 we imposed a time dependent physiological aortic pressure taken from Ref. [35] for all the scenarios (Fig. 4, right) because in presence of compensated MVR, the heart is able

to guarantee a physiological afterload [15, 60]. Finally, a no-slip condition is imposed on Σ_w in (2), prescribing the wall velocity coming from imaging.

To solve numerically the Eqs. (1) and (2) we considered first-order finite elements. Equation (2) was stabilized by means of a Streamline Upwind Petrov–Galerkin/Pressure-Stabilizing Petrov–Galerkin (SUPG/PSPG) scheme [63, 43]. We used the multiphysics high performance library $lifex$lifex [39] (https://lifex.gitlab.io/) based on the deal.II core [66] and developed in the iHEART project (https://iheart.polimi.it/). Hexahedral meshes were generated by using suitable algorithms developed in VMTK, in particular, for the mesh generation based on *TetGen*(*vmtkmeshgenerator*) and for the mesh refinement (*vmtkmeshrefinement*) [46, 61]. The average mesh element size was equal to 1.5 mm (1.9 mm) with a local refinement of 0.4 mm (0.35 mm) close to the mitral valve for H and R1 (R2). These values were chosen after a mesh convergence analysis performed on scenario H, which showed differences of the quantities of interest of at most 2% when the mesh was refined by a factor 10% Regarding the time discretization parameter, we set Δt=2.5×10^4 s, a value chosen after a convergence analysis showing that halving this value the quantities of interest did not change within a discrepancy of 2%. Numerical simulations were run on the cluster iHEART (Lenovo SR950 8 x 24-Core Intel Xeon Platinum 8160, 2100 MHz and 1.7TB RAM) available at MOX, Dipartimento di Matematica, Politecnico di Milano.

1.3 Numerical Results

We start our analysis by reporting the results in terms of geometry reconstruction in order to check the validity of the registration procedure, see “Description of the Scenarios” section. In particular, in Fig. 5, left, we reported for the ED frame the original surface obtained from MITK and that obtained by warping the reference configuration (i.e. the end systolic one) by the corresponding computed displacement field (we chose the ED surface because it is characterized in principle by the largest errors). These results underlined an excellent agreement between the two surfaces as

confirmed by the relative error of pointwise position, see Fig. 5, right, whose average value is 0.16%.

Then, we discuss the computational opening of the aortic valve. As stressed in "Geometric Reconstruction of the Left Ventricular Endocardium" section, for scenario H we could not simulate the isovolumic contraction, thus we began our simulation at the instant t_o=0 s just after the opening of the aortic valve. Instead, for R1 and R2 we observed that the pressure of the left ventricle was lower than the aortic one for t_o=0 s, due to mitral regurgitation, see Fig. 6A, top (ventricle and aortic pressures were calculated on slices showed in Fig. 6B, left). In particular, the opening of the aortic valve occurred at t_o=0.010 s and at t_o=0.01 6 s for R1 and R2, respectively.

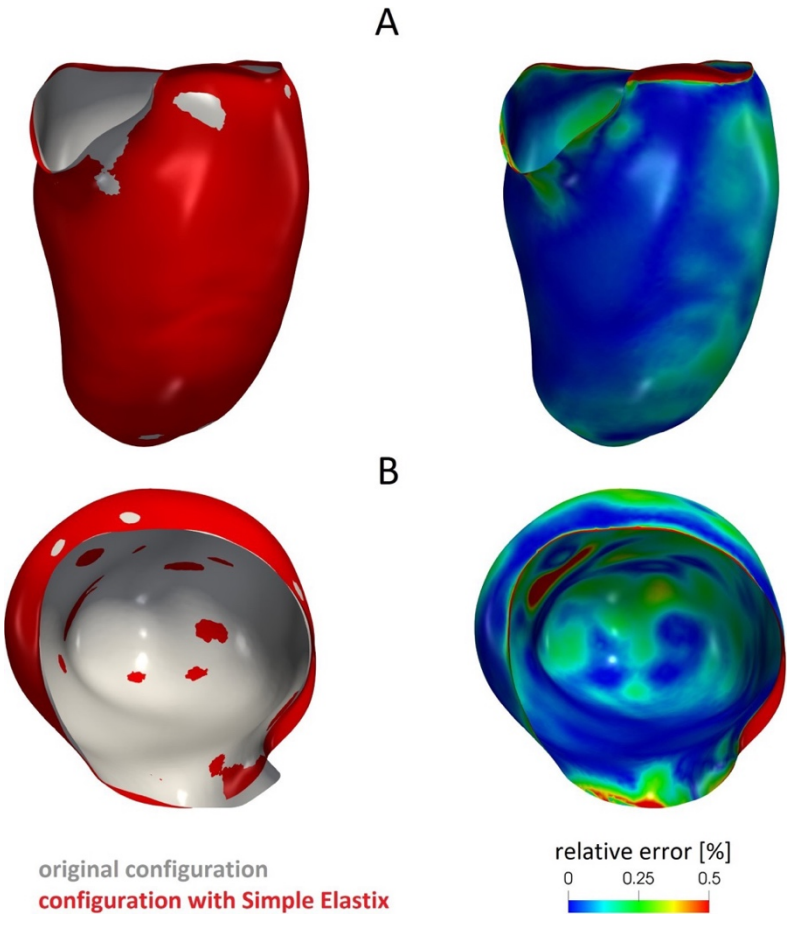

Fig. 5 For each of the two views *A, B*: comparison between the original end diastolic reconstructed surface and the one obtained after the registration procedure (left) and the corresponding relative error (right).

Figure 6A, top, also showed slightly larger values of the ventricular-aortic pressure drop for H with respect to R1 and R2, that featured very similar behaviours. This was also confirmed by the values reported in Table 1 where we computed the average in

time (from t_0 the closure instant t_c) of the pressure drop ΔP^{-} between the two slices of Fig. 6B, left.

To obtain a description of the spatial distribution of the pressure, in Fig. 7, we reported the pressure field in the whole domain at three representative instants t_1, t_2 and t_3. In particular, for H and R2 t_1=0.020t1=0.020 s, t_2=0.060, and t_3=0.200s, which correspond for R1 to t_1=0.017s, t_2=0.051 s, and t_3=0.170 s. We noticed that in all the scenarios and at all the three reported instants, the ventricular and atrial pressure was homogeneous in space. In particular, the ventricular pressure (as confirmed by Fig. 6A, top) was almost the same for the three scenarios, whereas the atrial one was (according to the outflow boundary conditions) much larger for the regurgitant cases. Regarding the closure of the aortic valve, from Fig. 6A we noticed that the closing stage of the aortic valve in H occurred at t_c=0.32s, while in R1 and R2 much earlier, i.e. at t_c=0.24 and at t_c=0.28 s, respectively. In Table 1, we reported the difference between t_c and t_o, representing the effective duration of the aortic ejection phase.

In Fig. 6A, middle, we reported the trend in time of the flow rate evaluated at the level of the LVOT (Fig. 6B, middle). For all the three curves, we could recognize two significant peaks, at t_{v1} (yellow points) and at t_{v2} (black points) and a final phase of deceleration.

In Fig. 6A, bottom, we reported the trend in time of the flow rate evaluated at the level of the mitral valve orifice (Fig. 6B, right). For R1 and R2, at t_o we had a local maximum due to the sudden opening of the aortic valve. After, both the curves started again to increase, reaching the global maximum at t_a (blue points) that was higher for R2.

From these curves we calculated some cardiac indices reported in Table 1: the SV and the regurgitant volume (RV), obtained by integrating in time the flow rates evaluated at the level of the LVOT and through the mitral orifice, respectively; the CO, given by the product between SV and the heart rate and the RF defined as the ratio between RV and the sum of the SV and RV. The value of the SV of the healthy case was compared with the one calculated in the preprocessing phase (i.e. by processing only Cine-MRI images), finding for the latter a value SV_{PP}=93.1 ml. The comparison suggested the presence of a small amount of volume across the valve equal to 1.1 mL, corresponding to 1.21% of the total volume. This highlights how the RIIS method led to very small

lacks of volume. To obtain a description of the the velocity patterns in the whole domain, in Fig. 8, the blood velocity field was represented on a 2D longitudinal slice to show the hemodynamics in the three scenarios. In particular, we considered three representative time instants: t_{v1}, t_a (t_a for H being the same as R2) and the instant of middle deceleration of the ventricle flow rate, $t_{dec}=t_{v2}+t_c/2$, see Fig. 6A. We observed that, as expected, in scenario H all the blood flowed in the aorta; instead, we noticed the formation of a *regurgitant jet* in the atrium for R1 and R2. At t_{v1}, in both the regurgitant cases the global velocity pattern was similar; the jet split in two different structures: one developing along the anterior leaflet (jet_1) and the other one arising directly from the free margin (jet_2) with a straighter direction. At t_a, also jet_1 assumed a straight configuration; in particular, in R2 the two jets collided close to the atrium outlet. In both R1 and R2 we also noticed that the velocities were elevated close to the wall of the atrium and that backflows formed at the outlet. At t_{dec}, the two jets split up in both the scenarios and, in correspondence of the atrial outlet, we noticed some fluctuations of the jets. In Table 1, we reported the maximum velocity magnitude U_{AV} and U_{MV} at the aortic valve plane and through the mitral valve orifice, respectively.

In Fig. 9, top, the ratio μ_{sgs}/μ between turbulent and physical viscosity was reported in the three cases at t_a.

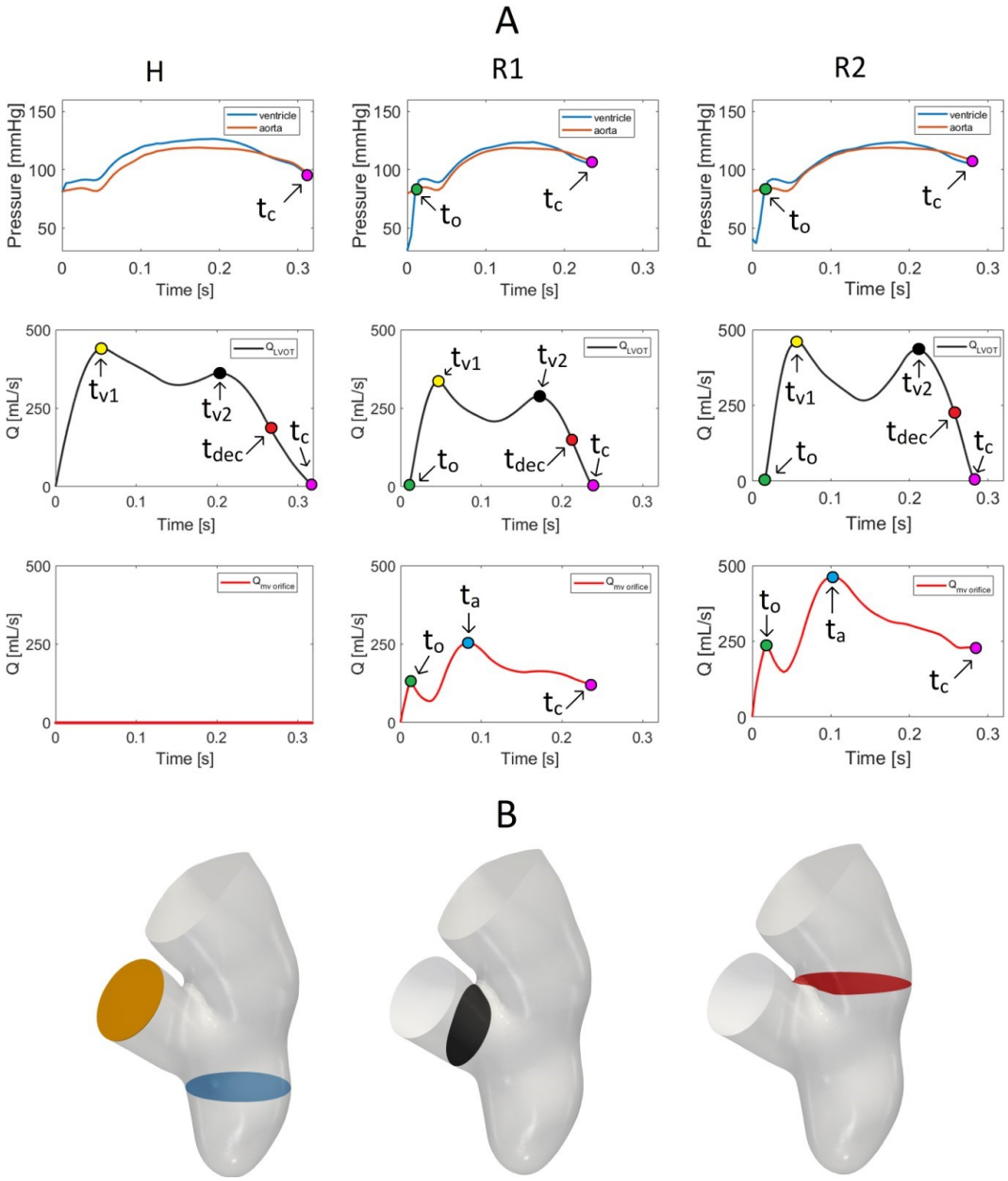

Fig. 6 Panel A, top: trend in time of the ventricle and aortic pressures (computed in the blue and orange slices reported in panel B, left); *to* is the time instant where the aortic valve opens; t_c is the time instant where the aortic valve closes. Panel A, middle: plot over the time of the flow rate at the level of the LVOT (computed in the black slice reported in panel B, middle); t_{v1} and t_{v2} are the peak instants and t_{dec} the instant of middle deceleration. Panel A, bottom: plot over the time of the flow rate at the level of the mitral valve orifice (computed in the red slice reported in panel B, right); *ta* is the time instant of the maximum flow rate. Panel B: sections of interest.

Scenario	ΔP [mmHg]	$t_c - t_o$	SV [mL]	CO [L/min]	RV [mL]	RF [%]	U_{AV} [m/s]	U_{MV} [m/s]	$\overline{R}$ [-]	$\overline{WSS_{MV}}$ [Pa]	$\overline{WSS_W}$ [Pa]
H	5.5	0.32	92	6.9	0	0	1.8	0.0	0.1	0.3	0.1
R1	2.6	0.22	50	4.5	40	44	1.3	6.5	2.4	5.4	2.9
R2	2.0	0.26	85	6.4	89	51	0.9	5.3	3.2	3.9	3.0

Table 1 Values of the quantities of interest computed for the three scenarios. ΔP : pressure drop between ventricle and aorta; *tc* - *to*: duration of the aortic ejection phase; *SV* : stroke volume; *CO*: cardiac output; *RV* : regurgitant volume; *RF* : regurgitant fraction; U_{AV} and U_{MV} : maximum velocity magnitude at the aortic valve and trough the mitral valve orifice; *R*: time average of the ratio between sub-grid and physical viscosity in the atrium; WSS_{MV} and WSS_W : time average of the trend in time of the WSS magnitude acting on selected regions of the mitral valve and of the atrial walls.

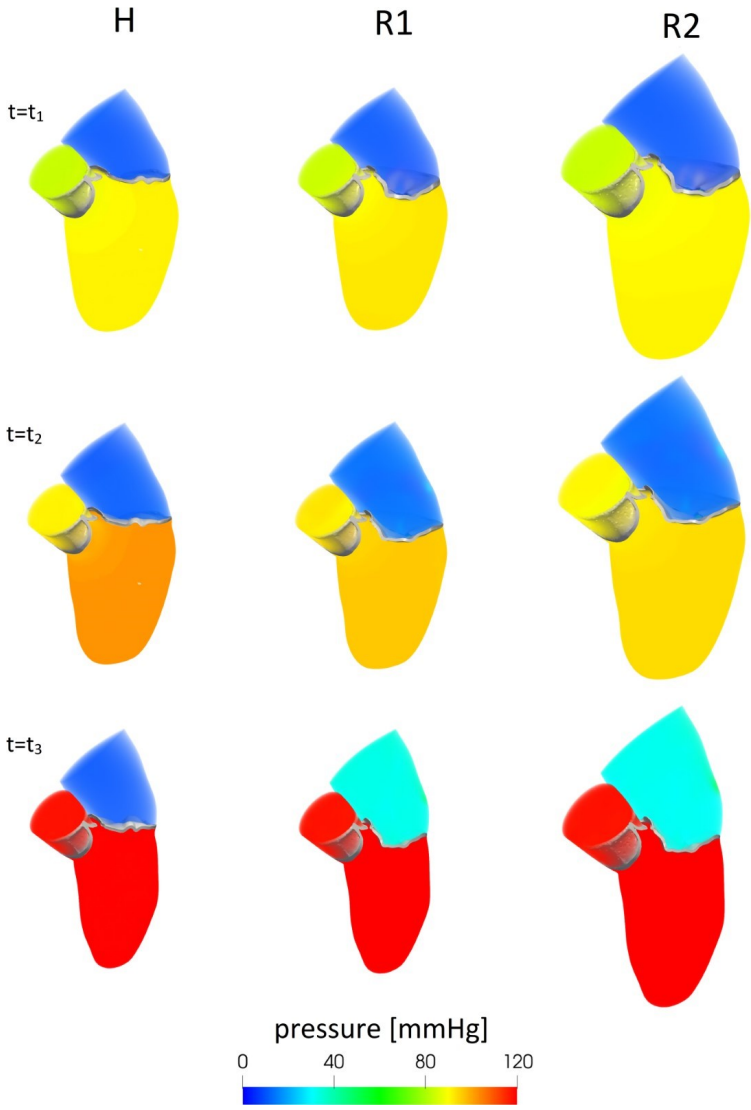

Fig. 7 Pressure field at three representative time instants, t_1, t_2 and t_3 (see the text for their definition), in the three scenarios.

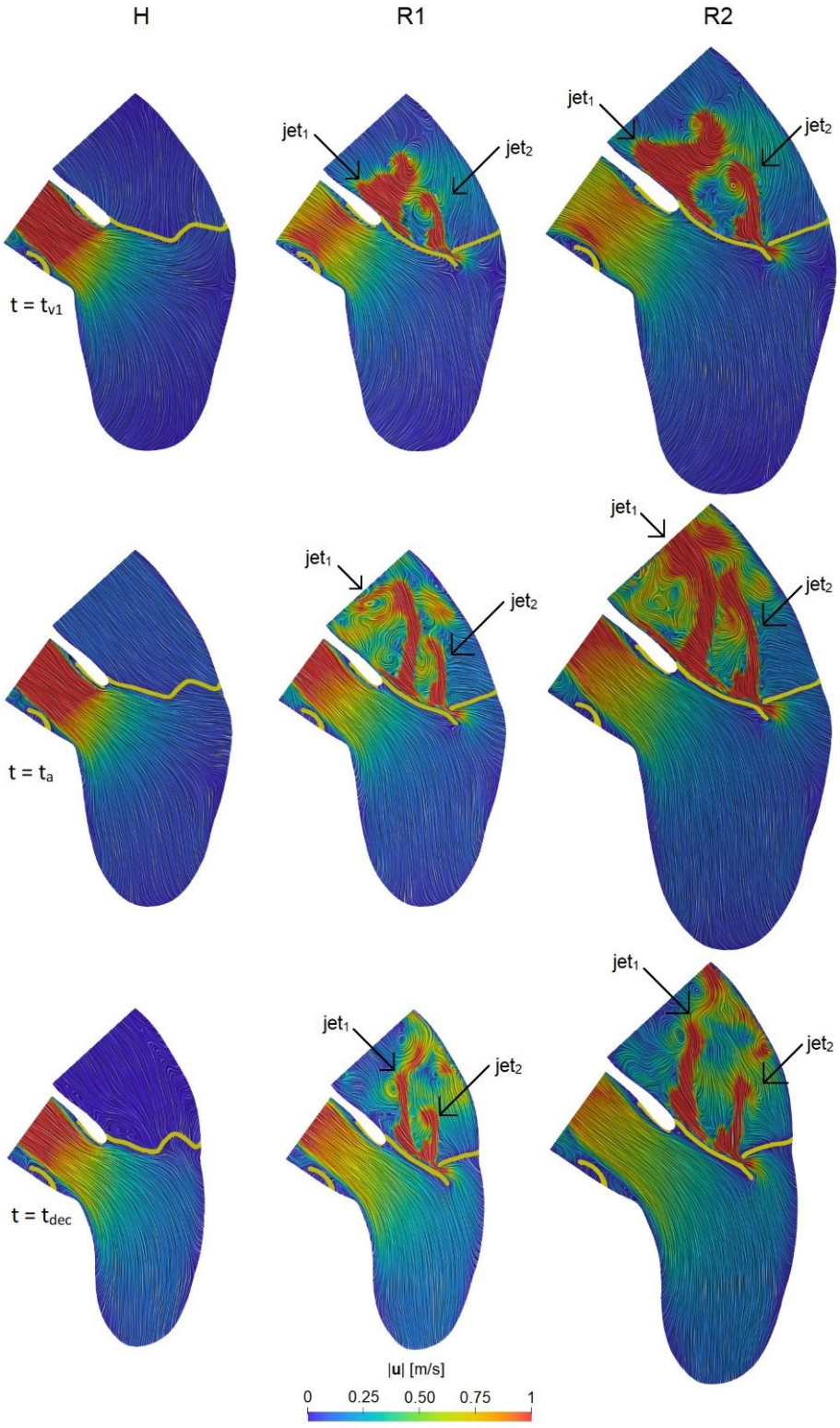

Fig. 8 Velocity magnitude at three time instants in the three scenarios. In yellow we reported a slice of the two valves. For the instants refer to Fig. 6A. For H we used the value of *ta* taken from R2.

From these results, we found elevated values of μ_{sgs} for R1 and R2 in the atrium, in particular in the regions with high velocities (see Fig. 8): at the level of the mitral valve orifice, where the sub-grid viscosity reached values also eight times greater than the value of the physical viscosity, and in the middle of the atrium, where chaotic and irregular velocity patterns were noticed. Similar patterns were found for the other time instants. Instead, as expected, scenario H did not feature transition to turbulence. In Fig. 9, bottom, we reported the trend in time of the average in the atrium of the ratio μ_{sgs}/μ for the regurgitant scenarios. In R2 we noticed a higher formation of turbulent viscosity as confirmed by Table 1, where we reported the average in time $\bar{R}$ of μ_{sgs}/μ, confirming the essential absence of transition to turbulence in the H case. In Fig. 10, top, we reported the streamlines through the mitral and aortic orifices and the magnitude of the WSSs on the mitral valve at instant *t*ata, for the regurgitant scenarios in three different views, namely A, B and C.

We noticed a hotspot of shear forces localized at the mitral orifice, where high velocities occurred (see also Fig. 8). We also observed, as expected, a chaotic regurgitant flow downstream the valve orifice, with swirling structures filling the atrium. Although the velocity patterns were very similar, these chaotic structures were more evident in R2 due to the higher values of the flow rate. In particular, we noticed the presence of the two regurgitant jets jet_1 (developing along the anterior leaflet, view B) and jet_2 (impinging against the atrial walls, views A and C).

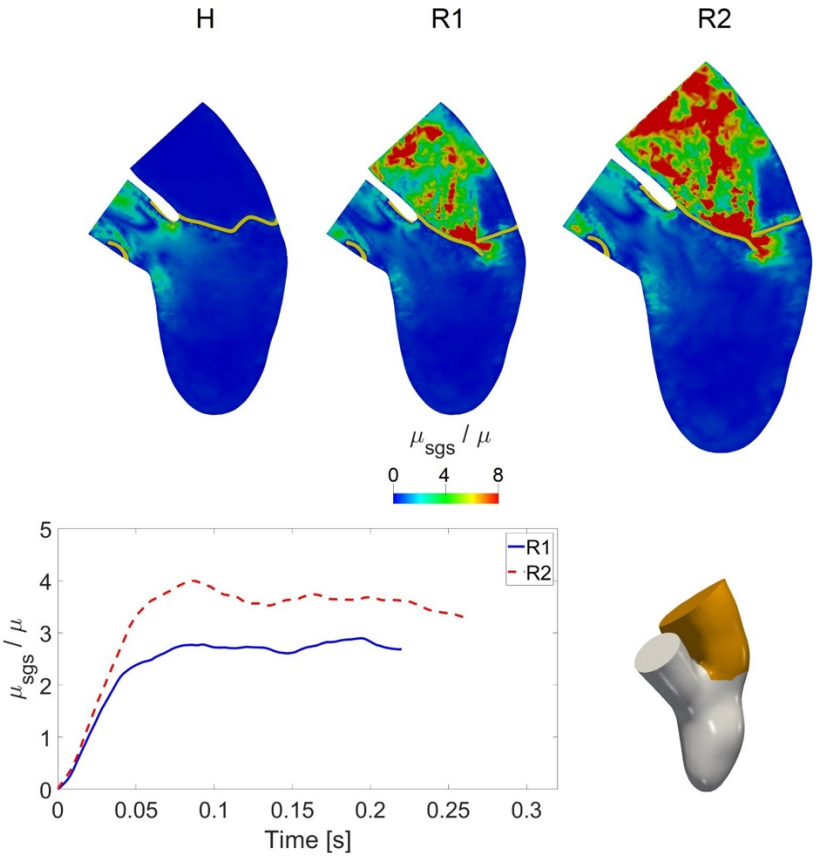

Fig. 9 Top: ratio between the turbulent viscosity μ_{sgs} and the physical viscosity μ in the three scenarios at t_a. For H we used the value of *ta* taken from R2. Bottom: trend in time of average (in space) in the atrium of the ratio between the turbulent viscosity μ_{sgs} and the physical viscosity μ for the regurgitant scenarios R1 and R2.

In Fig. 10, bottom, we reported a histogram showing the distribution of the WSS magnitude at t_a, clustered in three intervals, acting on the red region reported on the left. This region was selected as representative of elevated WSS and corresponds to the free margin and to a part of the anterior leaflet. We noticed that, even if the majority of the values fell in the range 2–4 Pa, more elevated values (>6 Pa) were found for a significant number of points, especially for R1. We also reported the average of the WSS in the red region as a function of time. We observed that R1 featured higher WSS values than R2. This was also confirmed by the values reported in Table 1, where we computed the corresponding average in time WSSMV.

In Fig. 11, top, we reported, for the regurgitant scenarios R1 and R2, the volume rendering of the velocity magnitude and the spatial distribution of the WSS magnitude at instant t_a, evaluated in the atrial region in two different perspectives. From this

figure we observed that in R1 and R2 the combined action of the two regurgitant jets jet_1 and jet_2 gave rise to two different zones of high WSS: the area where jet_2 impinged against the wall of the atrium (view A) and the area where jet_1 rubbed against the wall of the atrium adjacent to the anterior leaflet (view B, refer also to Figs. 8 and 10). In Fig. 11, bottom, we reported a histogram showing the distribution of the WSS magnitude at t_a, clustered in four intervals, acting on the two red regions reported on the left. These regions were selected as representative of elevated WSS and correspond to the areas where the regurgitant jets impinged against the atrial wall, see Fig. 11, top. We noticed that, even if the majority of the values fell in the range 3–6 Pa, more elevated values of the WSS (up to 12 Pa, or even more for R1) were found for a significant number of points. All these ranges resulted much higher than those of H where all the values fell in the interval 0.1–0.5 Pa. We also reported the average of the WSS in the two red regions as a function of time. In Table 1, we computed the corresponding average in time WSSW and the values were very similar for R1 and R2 and much higher with respect to H.

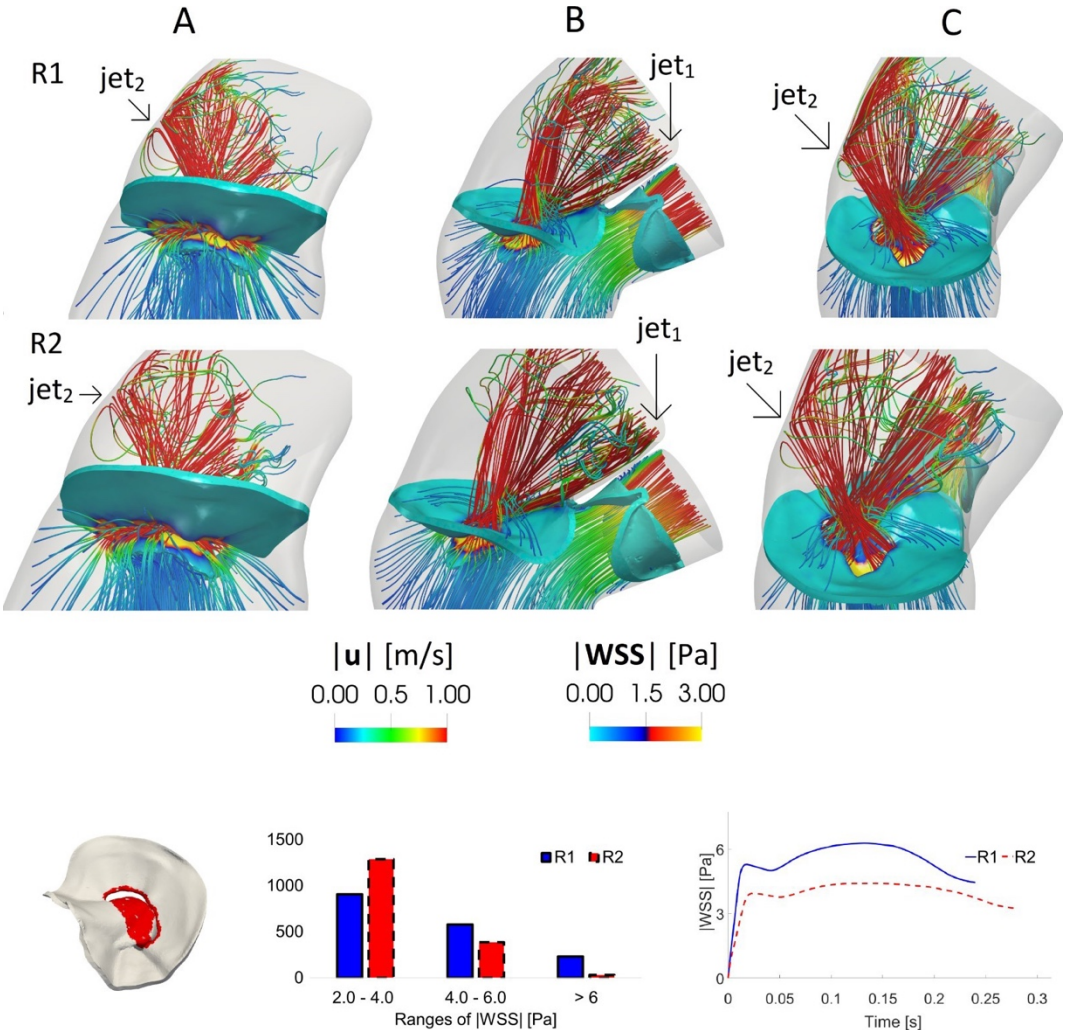

Fig. 10 Top: streamlines of the velocity magnitude through the mitral and aortic orifices and magnitude of the WSS on the mitral valve. Instant *ta*; three different views; R1 and R2 configurations. Bottom, left: in red the selected region with the points used to compute the histogram and the plot reported on the right. Bottom, middle: distribution of the WSS magnitude acting on the red region at *ta*. Bottom, right: trend in time of the average (in space) of the WSS magnitude acting on the red region.

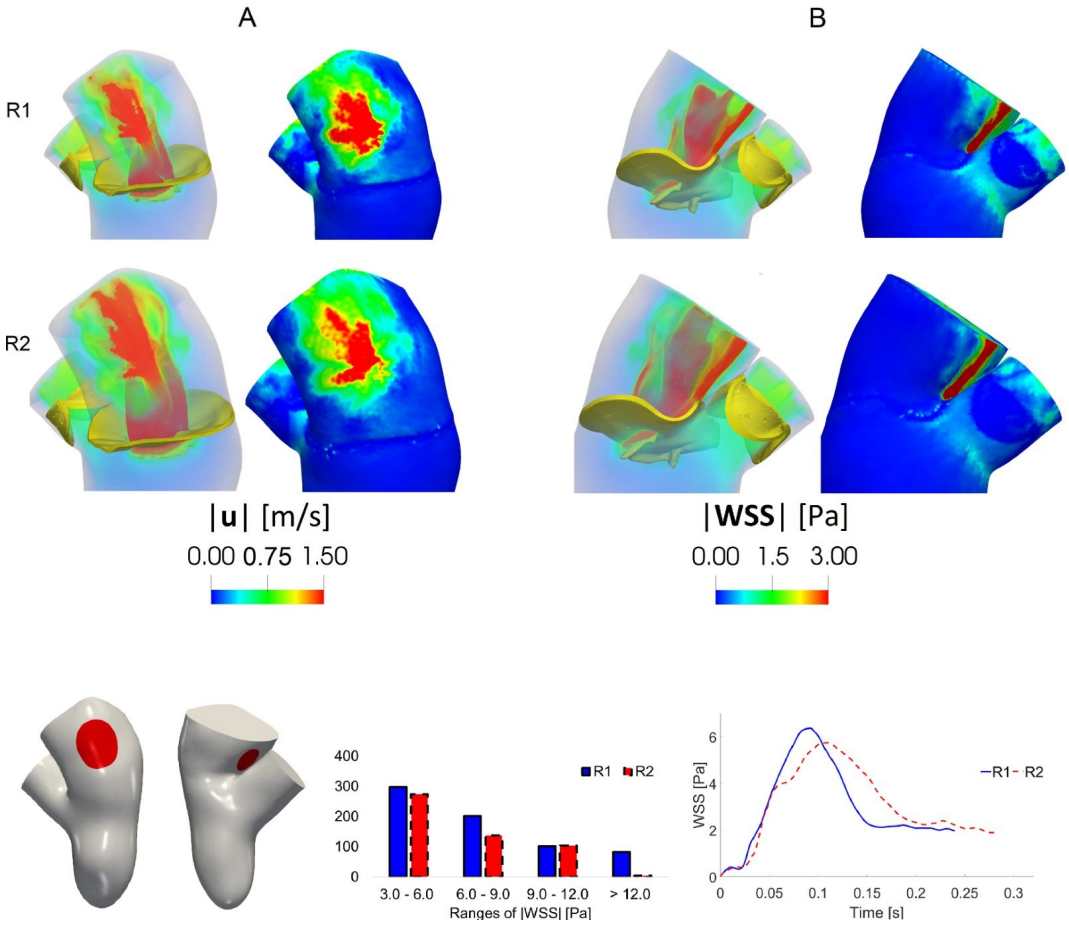

Fig. 11 Top: for each of the columns A and B: volume rendering of the velocity magnitude (left) and spatial distribution of the WSS magnitude (right). Time *ta*. Bottom, left: in red the selected regions with the points used to compute the histogram and the plot on the right. Bottom, middle: distribution of the WSS magnitude acting on the red regions at *ta*. Bottom, right: trend in time of the average (in space) of the WSS magnitude acting on the red regions.

1.4 Discussion

In this work we performed an image-based computational study to analyze the hemodynamics in presence of a healthy (H) and regurgitant valve with either increased heart rate (R1) or dilated left ventricle (R2). These two phases represent two different mechanisms the heart employs to compensate the decreasing of the CO due to MVR. This process is known as *heart remodeling*, however what is still unclear in the literature is the interplay between all the factors involved (such as pressure, velocity,

volumes and shear forces) [59]. First, analysing the ventricular-aortic pressure drop which represents and quantifies the force generated by the ventricle to win the aortic resistances, we found that in R1 and R2 the ventricle was not able to provide the same pressure drop between ventricle and aorta of the H case (Figs. 6A, top, 7 and values of ΔP^{-} in Table 1). The consequence of lower values of pressure drop in the regurgitant scenarios was the shortening of the aortic ejection phase interval $t_c - t_o$, with a delay of the opening of the aortic valve at t_o and an advance of the closing time t_c (see Table 1). This time interval could be of interest for a better knowledge of the pathology and also useful from the clinical point of view, since it may help the physician in the quantification of the degree of MVR, as done in some clinical studies [1]. We also observed from Fig. 7 almost the same ventricular pressure among the three scenarios, despite the increased atrial pressure in the regurgitant cases. This suggested that the ventricular pressure was mainly driven by the wall displacement (which indeed was the same for the three scenarios) rather than by the health state of the mitral valve.

Second, as for the ventricular-atrial pressure drop, we found that it was the same for the two regurgitant cases (see Fig. 7), suggesting that it is mainly determined by the shape and dimension of the regurgitant orifice rather than by the overall conditions (heart rate, dilation,...).

Regarding our choice of opening instantaneously the aortic valve in the regurgitant scenarios, we observed that when it opened, the blood started to be ejected into the aorta with a force that is proportional to the positive pressure drop between the ventricle and aorta, but anyway too small to lead to potentially unphysiological values of the velocity. This is confirmed by Fig. 6A, left and middle, where we noticed, at the first time instants of the aortic valve opening, physiological values and trends of the ventricular pressure and flow rate, suggesting that the instantaneously opening of the aortic valve did not have so much influence on the blood velocity and pressure.

In scenario H all the blood was ejected into the aorta with a flow peak at t_{v1} of 440 mL/s and a maximum ventricle pressure of 126.5 mmHg; these values were consistent with standard physiological data [49, 68]. Instead, in R1 and R2 part of the blood flowed back to the atrium. In all the scenarios, the ventricular flow rate featured two peaks (Fig. 6A, middle). This specific behavior was previously found in other studies [35, 9, 30].

From the flow rates through the aortic and mitral valve we calculated some cardiac indices (see Table 1), used by the physicians to elaborate the diagnosis. In R1 and R2 we noticed that such indices fell into the physiological ranges [20] despite the reduced CO with respect to H, highlighting the ability of the system to compensate for MVR by increasing the heart rate and/or augmenting the ventricular dimensions. In particular, in R1 the increasing of the heart rate provided more blood flow to aorta than to left atrium (regurgitant fraction RF<50%). Instead, in R2 the ventricle dilation allowed to sustain a physiological value of SV, even if the volume of blood returning to the left atrium was larger (RF>50%).

Regarding blood velocity, in scenario H the maximum velocity magnitude U_{AV} through the aortic valve was 1.8 m/s, a value comparable with those found in other studies [6, 82], while in the regurgitant scenarios the velocity values decreased to 1.3 and 0.9 m/s for R1 and R2, respectively. These values shown a correlation with the values of RV and RF reported in Table 1, in particular, larger values of regurgitation indices were characterized by smaller values of U_{AV}. This is in accordance with the decreased flow rate through the aortic valve in presence of MVR. Notice, however, that for R2 U_{AV} is smaller than R1, despite the aortic flow rate, due to the dilation, is larger (see Fig. 6, middle, right).

Moreover, in R1 and R2 we found chaotic velocity patterns in the atrium (Fig. 10) with values of 6.5 and 5.3 m/s for the regurgitant maximum velocity U_{MV} trough the mitral valve, respectively. These values were similar to others found in literature [89, 64, 70]. Interestingly, we noticed that UMV was higher in R1, despite lower values of RV and RF than R2. This apparently counter-intuitive behavior is due to the smaller mitral orifice regurgitant area experienced by the blood flow in R1. Furthermore, in both scenarios, the regurgitant jet split in two different structures, one of which (jet_1) developed along the anterior leaflet (see Figs. 8 and 10). This behavior was in accordance with the Carpentier's functional classification [14, 45, 72], intensively used by cardiologists for diagnosis purposes, for which, in case of MVR due to a prolapse, the jet is directed away from the pathological leaflet, in our case the posterior one [72].

We also noticed that, in the regurgitant cases, the velocity patterns in the atrium were comparable, due to the similar shape of the mitral orifices, despite their different size.

Thus, the dilation of the geometry did not affect the distribution and the direction of the retrograde flow leading to an impingement of blood against the atrial wall in the same areas.

The formation of the regurgitant jet in the atrium led to high values of the subgrid viscosity in the turbulence model (Fig. 9 and turbulence index $\bar{R}$ in Table 1) suggesting that the formation of transition to turbulence in the left atrium could occur during systole in the regurgitant cases, especially in the dilated scenario.

MVR also yielded to high values of WSS on the mitral valve and on the atrial wall (see Figs. 10, 11 and Table 1), especially if compared with the values computed for the healthy case H and with the physiological range (0.4–1.2 Pa) found in the literature [52, 80]. It is well established in the literature that the WSS influence the cardiovascular development and remodeling [4] and our results highlighted that both in R1 and R2 the combined action of the two jets gave rise to high values of the shear forces concentrated in the same areas of the left atrium (Fig. 11 and the values of $\overline{WS_{SW}}$ in Table 1). This could be relevant since the atrium is stressed by the regurgitant jets in the same areas during the heart remodeling, suggesting that in MVR due to a leaflet prolapse the left atrial size should be monitored by investigational tests in order to prevent the risk of an excessive dilation of the wall leading potentially to atrial fibrillation [79, 13, 71], the most common complication of the MVR, or in more rare cases to aneurysm formation [83, 87].
In the regurgitant cases we also noticed elevated values of WSS on the mitral valve leaflets, in correspondence of the free margin (Fig. 10 and the values of $\overline{WSS_{MV}}$ in Table 1). While the action of the WSS on the vascular tissue is quite understood, its effects on the valvular tissue are still under debate [8]. A shared conjecture is that the repeated action of the shear forces at every cardiac cycle could damage the endothelial valve tissue and trigger numerous active mechanisms resulting in potential valve degeneration and calcification [8].

1.5 Special Considerations and Limitations

The main outcomes and contributions of the present study could be summarized as follows:

(1) We showed how it is possible to build a framework to obtain virtual scenarios in the moving ventricle to analyze systolic hemodynamics, without the need of using a FSI model and by using instead dedicated dynamic images of the left ventricle and of the mitral valve; At the best of our knowledge, we described, for the first time, the presence of transition to turbulence in the atrium during systole in the regurgitant cases by means of a computational study;
(2) We compared two possible regurgitant scenarios providing a quantitative comparison of different hemodynamic quantities, highlighting the ability of the system to compensate MVR and recover a physiological CO (albeit slightly smaller than the healthy case);
(3) We quantified the chaotic velocity pattern in the atrium in the regurgitant cases highlighting the presence of two distinct jets; moreover, we assessed the WSS magnitude on the mitral valve and atrial wall, focusing on the increase of viscous forces due to regurgitation.

Some limitations characterized this study:

(1) Starting from a ventricular geometry segmented from MRI, we filled the missing geometric data by considering a template for the left atrium and the aortic valve and a flow extension for the aorta. We notice however that such information are not in general visible from standard short-axis MRI acquisitions. For this reason, we are currently investigating the integration of short axis images with other MRI acquisition series that include also the left atrium and the aorta. Another geometric limitation consists in the smoothed ventricular endocardial reconstruction which did not include the papillary

muscles, whose effect should be investigated in order to assess their influence in the quantities of interest of this study.

(2) We expanded harmonically the ventricular displacement to the wall of the left atrium and aorta. With this choice we neglected the dilation of the left atrium and aorta during the ventricular systole. This point is currently under scrutiny, to understand how to include plausible dilation motions of aorta and left atrium, following e.g. the strategy proposed in Ref. [90].

(3) We simulated only systole, including the isovolumic contraction for R1 and R2, since MVR is a pathology involving mostly this phase. Further investigations to extend our study to the diastolic phase will be mandatory in order to assess the effects of MVR during this phase and to remove the influence of the null initial condition more heartbeats should be performed. Notice that, we had nine systolic frames at our disposal, but in fact we worked only with six of them, and discarded three instants, since they were affected by a huge amount of noise that yielded a reconstruction that was incompatible with the other six, with a consequent irregularity of the displacement field and distortion of the mesh during its movement. Notice that these three frames were intermediate ones, thus we guaranteed to work with the patient specific SV.

(4) We are aware that, in the clinical setting, the degree of MVR, for the same type of valvular disease, is extremely variable, depending upon several variable factors, such as heart rate, ventricular contractility, pre-load and after-load. Our current study was limited to the description of hemodynamics considering only one degree of MVR and two possible scenarios (increased heart rate and increased ventricular dimensions), maintaining all other parameters unchanged in all groups. The effects of different degrees of MVR on the hemodynamic quantities could be of clinical interest and investigated in future works, both conducting parametric studies accounting for a synthetic reduction/dilation of the mitral orifice, or analyzing several patients with different regurgitation severity.

(5) In this work, we created three different virtual scenarios starting from a reference case. This is a well accepted strategy when one wants to compare the effect of a single change (in our case mitral regurgitation) on some outputs (see

e.g. Ref. [35] for the case of mitral valve prolapse or Ref. [29] for different SAM degrees). The definition of these scenarios has the advantage of isolating specific pathological features of MVR from concurrent ones. The comparison between H and R1/R2 allowed us to assess the effects of the mitral regurgitation solely (together with the functional changes that this pathology implies, i.e. increased heart rate or dilation, according to the case) without introducing concurrent effects due to the different patients' anatomies. Accordingly, we considered a single geometry, obtained from a single patient.

After validation of the model, we performed a computational image-based study of blood dynamics in the whole left heart, both in a healthy subject and in a patient with mitral valve regurgitation (MVR). We proceeded as detailed in the next chapter.

2. Turbulent blood dynamics in the left heart in presence of mitral regurgitation: a computational study based on multi-series cine-MR images

2.1 Introduction

We elaborated multi-series cine-MR images with the aim of reconstructing the geometry and the corresponding motion of left ventricle, left atrium, mitral and aortic valves, and aortic root of the subjects. This allowed us to prescribe such motion to computational blood dynamics simulations where, for the first time, the whole left heart motion of the subject is considered, allowing us to obtain reliable subject-specific information. The final aim is to investigate and compare between the subjects the occurrence of turbulence and the risk of hemolysis and of thrombi formation. As already highlighted, the pathologies affecting the left heart (LH) are the most common cause of death in the world [91]. One of these is mitral valve regurgitation (MVR), a condition leading to a formation of a regurgitant jet in the left atrium during the systolic phase due to an incomplete closure of the mitral valve leaflets. The formation and the development of the regurgitant jet may give rise to: i) presence of highly disturbed or even turbulent atrial flow that can lead to hemolysis in the atrium [92, 93] and ii) washing out of stagnant blood in the atrium that could prevent thrombi formation [94]. These phenomena are difficult to describe and quantify in the clinical practice. On the one hand, although clinical measures such as the *regurgitant volume* and the *regurgitant fraction* may provide significant information about the global cardiac function, they are not able to capture local features such as 3D velocity distribution and wall shear stresses [95, 96]. Moreover, the space and time resolution of the available imaging techniques, such as Four-Dimensional Flow Magnetic Resonance Imaging (MRI) or Phase-Contrast MRI, is not nowadays enough accurate to capture small-scales features as recirculation areas, regions of transition to turbulence, and small coherent structures [97]. In this respect, computational methods can non-invasively provide quantitative information about the local pressure gradients, the velocity patterns, and the shear forces, contributing to a better understanding of the cardiovascular system [98–104]. In particular,

computational models applied to LH have contributed to a better knowledge of the cardiac patho-physiology [105– 113] and to model and predict the outcomes of valve prostheses or surgical interventions [114–117]. Such methods can be broadly grouped in two categories: *Fluid Structure Interaction* (FSI) models [106, 110, 112, 113] and *Computational Fluid Dynamics (CFD) with prescribed wall motion*. For the latter, the prescribed motion could be obtained either from an electromechanics simulation [118–122] or by dedicated time-resolved medical images (*Dynamic Image-based CFD*, DIB-CFD). The latter approach has become, in the last decade, a valid alternative to FSI models when sufficiently detailed dynamic medical images are available [123–130]. In particular, regarding DIB-CFD studies investigating MVR, we mention works where the authors tested and compared different types of mitral valve prolapse [131], different degrees of MVR [132], different functional changes of the ventricle and atrium in response to MVR [133] and different effects of MVR in the right heart [134]. However, no one of these studies was performed on a fully patient-specific LH geometry and displacement (ventricle + atrium + mitral valve + aortic valve + aortic root). Moreover, none of them investigated the transition to turbulence, nor the risk of hemolysis and the prevention from thrombi formation in the atrium.

In this context, the present work has two principal aims:

i. perform a DIB-CFD simulation of the whole heartbeat on a healthy subject and on a patient with MVR;
ii. investigate the transition to turbulence, the risk of hemolysis formation, and the prevention from thrombi formation with respect to the healthy subject.

The main improvements and novelties of this work are:

i. a fully LH patient-specific DIB-CFD simulation with imposed motion of ventricle, atrium and aortic root together with the geometries of the mitral and aortic valve, all reconstructed from multi-series (i.e. Long-Axis, Short-Axis, and mitral valve Rotated series) cine-MR images during the whole heartbeat. In particular, unlike the works of [125, 128], we included both the aortic and mitral valve geometries;
ii. the investigation of the transition to turbulence in the MVR case, so far investigated only in physiological cases [125,128];

iii. the study of the risk of hemolysis in the atrium and the prevention from thrombi formation with respect to the healthy subject. These phenomena, so far, has not been investigated in presence of native valve with MVR by means of a computational study.

Moreover, the novelty with respect our previous work [133], is the simulation of the whole heartbeat. The significance of our results has been supported by the validation with Echo Colour Doppler (ECD) measures in the healthy subject and by a qualitative comparison with a cine-MRI flow pattern in the MVR case.

2.2 Methods

In this section, we first described the multi-series cine-MR images at disposal and the acquisitions of the ECD measurements; after, we detailed the reconstruction techniques used to obtain the patient-specific geometries and displacements of the left ventricle (LV), left atrium (LA), aortic root (AR), mitral valve (MV), and aortic valve (AV); then, we briefly reported the mathematical and numerical methods used in this work; finally we introduced the quantities of interest that has been analyzed in the Results section.

2.2.1 Available cine-MR images and ECD acquisitions

Cardiac multi-series cine-MRI data of two subjects were always provided by the Department of Radiology of University Hospital of Verona, Verona, Italy. Ethical review board approval and informed con- sent were obtained from all subjects. In particular, we acquired dynamic images, consisting of 30 acquisitions per heartbeat, of a healthy subject (H) and of a patient with a severe MVR due to a posterior leaflet prolapse (R). All the subjects were male. In Table 2, we reported some information about the two subjects, including the heart rate, height, weight and body surface area (BSA) [135].

Data of the two patients

Patient	Heart rate [BPM]	Height [m]	Weight [kg]	BSA [m^2]
H	66	1.93	84	2.14
R	75	1.84	105	2.28

Table 2 For each patient, we reported the values of heart rate, height, weight and BSA.

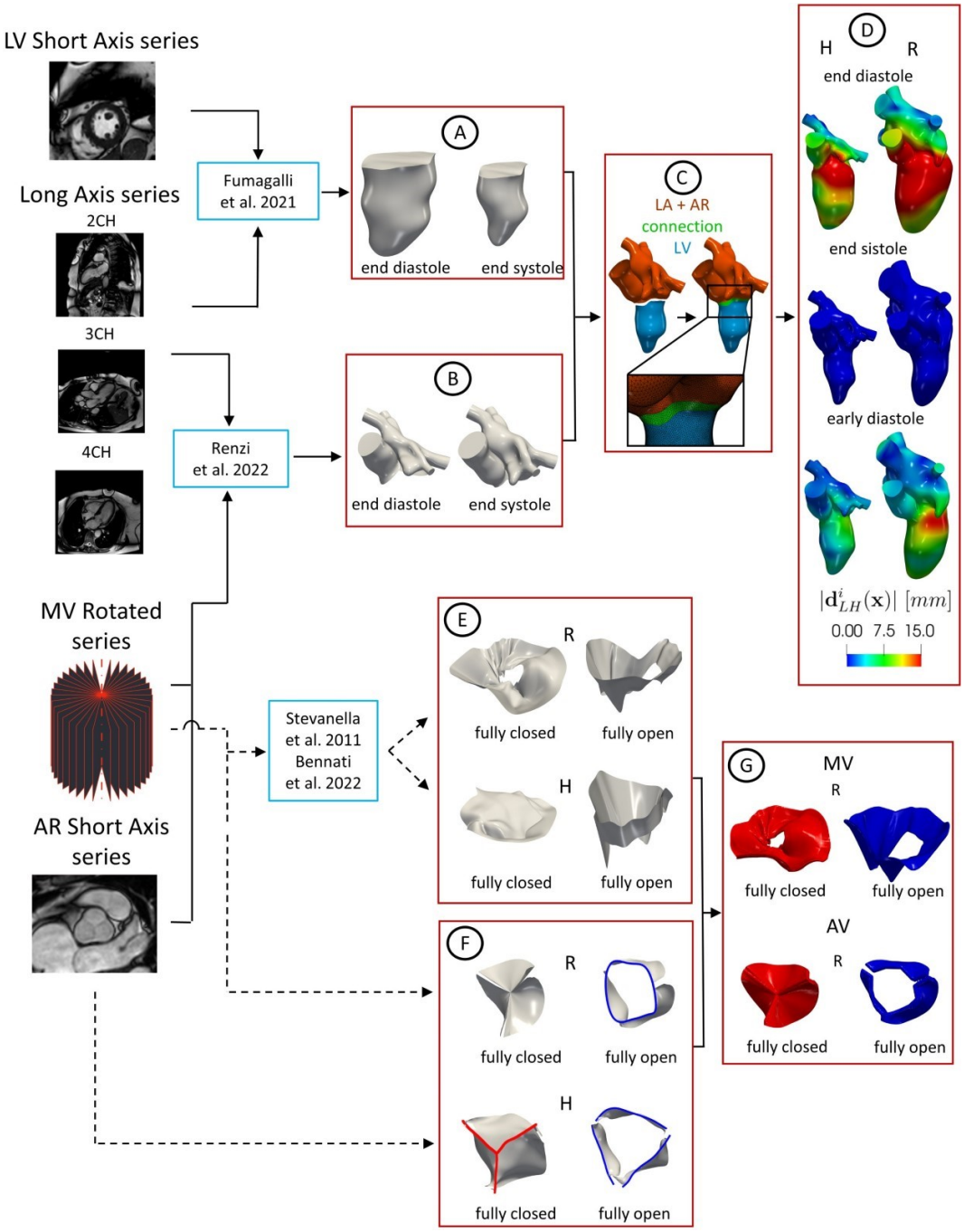

Fig. 12 Flow chart to reconstruct the geometries of LH and valves and their displacements. Continuous lines refer to the steps followed to reconstruct the LH walls and the dashed lines to the reconstruction of the valves. A: geometric reconstruction of the LV endocardium for all the 30 frames by adopting the strategy described in [130] (here we reported the geometries at two representative frames as an example). B: geometric reconstruction of AR and LA for all the 30 frames by adopting the strategy proposed in [136] (two representative frames reported as an example). C: creation of a connection to merge .

The acquisitions were performed with the Achieva 1.5T (TX) - DS (Philips, Amsterdam, Netherlands) technology. Specifically, for each patient, we have at disposal different acquisitions: the Short Axis series of LV, the Long Axis series and the Rotated series of MV (see [35] for further details). Moreover, for subject H we have at disposal also the Short Axis series of AR, consisting in volumetric series made of 4 slices with thickness and distancing of 8 mm along the aortic root main axis, with a spatial resolution of 1 mm and time resolution equal to 30 frames/cardiac cycle; see Figure 12, left. After the image acquisitions, patient R underwent to a surgical operation to restore a correct heart function.

We point out that the Long-Axis series and the Short-Axis series of LV are standard cine-MRI data that are routinely acquired in the clinical procedure. Instead, the Short-Axis series of AR and the Rotated series of MV represent ad hoc advanced cine-MRI acquisitions.

After the cine-MRI acquisitions, subject H underwent to ECD measurements with a EPIQ CVx ultrasounds scanner and linear 8MHz probe (Philips Ultrasound, Bothell, WA). The velocity measures were acquired at the peak instants at three different locations: P1: 1 cm upstream the AV base; P2: 1.6 cm downstream the MV annulus; P3: 5.5 cm far from the the LV apex, see Figure 13A.

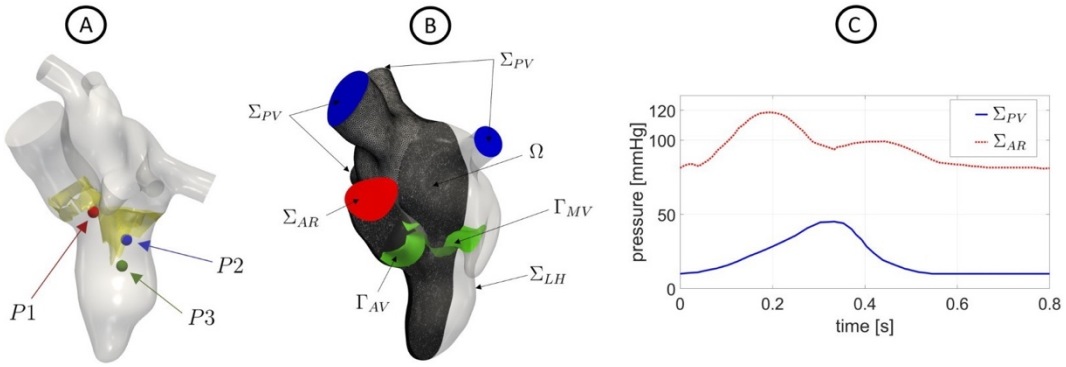

Fig. 13 A: Location of the points where ECD measures were acquired. B: Computational domain **Ω** with its boundaries. In green we reported the aortic and mitral valves Γ_{AV} and Γ_{MV} . The computational mesh of patient R is also displayed. C: trend in time of the pressures imposed at Σ_{PV} (for scenario R) and Σ_{AR} (for H, the curve at the AR outlet has been suitably adapted based on its heartbeat).

2.2.2 Geometric reconstruction of the left heart internal wall surfaces

In this section, we describe a novel framework to reconstruct the LH geometry and displacement. This is based on combining two different reconstruction techniques proposed so far for LV and for LA/AR, respectively. The entire procedure is represented in Figure 12, from step A to step C.

Regarding the LV reconstruction, we adopted the strategy described in [122]. Starting from the Short-Axis series of LV, we merged them with the Long-Axis acquisitions (2CH, 3CH and 4CH views) to obtain new enhanced time-dependent series of volumetric images with a uniform space resolution of 1 mm in all directions. From these enhanced images, we segmented and reconstructed the shape of the LV endocardium in all the 30 frames by using the algorithm proposed in [129] and implemented in the Medical Image Toolkit (MITK) open-source software (www.mitk.org), see step A in Figure 12.

After, we reconstructed the shape of AR and LA in all the 30 frames by using a cine-MRI multi-image based reconstruction algorithm, proposed in [127] for the right heart and implemented in the Vascular Modeling Toolkit (VMTK) (www.vmtk.org)[130, 131]. This is based on manually tracing the contours of AR and LA from the Rotated series of MV, the Long Axis series, and, when available, the Short Axis of AR. For each frame, a 3D point cloud was obtained, that was turned into a surface mesh of triangles, see step B in Figure 12.

After, we reconstructed the shape of AR and LA in all the 30 frames by using a cine-MRI multi-image based reconstruction algorithm, proposed in [127] for the right heart and implemented in the Vascular Modeling Toolkit (VMTK) (www.vmtk.org)[130, 131]. This is based on manually tracing the contours of AR and LA from the Rotated series of MV, the Long Axis series, and, when available, the Short Axis of AR. For each frame, a 3D point cloud was obtained, that was turned into a surface mesh of triangles, see step B in Figure 12.

Then, for each reconstructed frame, we merged the geometry of LV with the AR and LA ones in MeshMixer (https://www.meshmixer.com) to obtain the final surface mesh of LH, see Figure 12, step C. Subsequently, we registered the displacement of each frame with respect to the end systolic configuration by exploiting the non-affine B-splines algorithm implemented in the Elastix open source library

(http://elastix.isi.uu.nl) [132] used and validated in [125]. The output is the surface mesh of LH at the end systolic instant, where the displacement field $d^i_{LH}(x)$, i = 1,..., 30, is defined for all the 30 frames. In Figure 12, step C, we reported the magnitude of $d^i_{LH}(x)$ at three representative frames.

2.2.3 Geometric Reconstruction of the valves

In this section, we describe the geometric reconstruction of the valves. The entire procedure is reported in Figure 12, from step D to E. Regarding the MV reconstruction, starting from the Rotated series of MV, we reconstructed its shape in the fully closed (FC) and fully open (FO) configurations by using the method proposed in [128] (see step D in Figure 12), where the authors performed structural analysis, see also [133]. This method is based on tracing the valve leaflets in each plane to obtain a 3D point cloud that was after fitted with a B-Spline and then turned into a surface mesh of triangles in Matlab (www.mathworks.com), see [125] for details, where this MV reconstruction procedure has been, for the first time, applied to DIB-CFD simulations. Concerning AV, the cine-MRI images at disposal did not allow a complete reconstruction of the patient-specific leaflets, thus we exploited a FO aortic valve template taken from the Zygote solid 3D heart model, a complete geometry reconstructed from CT scans representing an average healthy heart (https://www.zygote.com). We adapted it to our patients by exploiting the available structures that we were able to reconstruct. In particular, the FO configuration was geometrically deformed in order to match the annulus with that segmented from our cine-MRI images (from the AR Short Axis series for subject H and from the Rotated series of MV for patient R), see step F in Figure 12. The AV FC configuration was obtained for subject H by means of the same procedure used for FO, while for patient R it was obtained by exploiting algorithms based on the closest-point distances [131], see step F in Figure 12.

2.2.4 Mathematical and numerical modeling

Blood was modeled as an incompressible, homogeneous, Newtonian fluid with density $\rho = 1.06 \cdot 10^3$ kg/m^3 and dynamic viscosity $\mu = 3.5 \cdot 10^{-3}$ Pa · s, described by the

Navier-Stokes (NS) equations, see [134,135]. To solve NS in moving boundaries we used the Arbitrary Lagrangian Eulerian (ALE) framework [136]. To treat the presence of the valves, we used the Resistive Immersed Implicit Surface (RIIS) method [137,138] and to evaluate the transition to turbulence, we employed the σ -LES method proposed for ventricular blood dynamics [139] and successfully used in different hemodynamic applications [140,141]. The entire method is described in a previous study [125]. In particular, the displacement of LH $\mathbf{d}^i_{LH}(\mathbf{x})$ is used to compute the wall velocity to prescribe as boundary condition for the NS equations. Since $\mathbf{d}^i_{LH}(\mathbf{x})$ has been obtained only at the MRI acquisition times (i = 1,..., 30), we employed a spline interpolation to obtain $\mathbf{d}^i_{LH}(\mathbf{x},t)$ for all $t \in [0, T]$ where T is the duration of the heartbeat, equal to 0.9 s for subject H and 0.8 s for patient R, see Table 1. According to the ALE framework, at each time, the fluid domain $\Omega(t)$ is obtained by extending $\mathbf{d}^i_{LH}(\mathbf{x},t)$ into Ω through the solution of a linear elastic problem [142].

The entire domain with its boundaries is displayed in Figure 13B. In particular, Σ_{LH} represents the internal wall surfaces of LH, Σ_{AR} and Σ_{PV}, the final sections of the aortic root and pulmonary veins, respectively. In green, instead, we reported the surfaces of the aortic ΓAV and mitral valve Γ_{MV}.

Thus, the ALE NS equations in the known domain $\Omega(t)$ are solved to find the pressure p and the blood velocity u:

$$\begin{cases} \rho\dfrac{\partial \mathbf{u}}{\partial t} + \rho(\mathbf{u}-\mathbf{u}_{ALE})\cdot\nabla\mathbf{u} - (\mu+\mu_{sgs})\Delta\mathbf{u} + \nabla p + \sum_{i=AV,MV}\dfrac{R_\Gamma}{\varepsilon_\Gamma}(\mathbf{u}-\mathbf{u}_{ALE})\delta_{\Gamma_i} = \mathbf{0} & \text{in } \Omega(t), \\ \nabla\cdot\mathbf{u} = 0 & \text{in } \Omega(t), \\ \mathbf{u} = \dfrac{\partial \mathbf{d}_{LH}}{\partial t} & \text{on } \Sigma_{LH}(t), \end{cases} \quad (1)$$

with a null initial condition in $\Omega(0)$. μ_{sgs} is the sub-grid viscosity of the σ -model [139], whereas $\delta_{\Gamma i}$ is a smoothed Dirac delta function representing a layer, with thickness $2\varepsilon_\Gamma$, around the surface of the valve Γ_i, i = AV,MV, [121,138], and R_Γ is a resistance coefficient. In our numerical experiments, we set $R_\Gamma = 10^5$ kg/m · s and $\varepsilon_\Gamma = 0.75$ mm [125, 143].

The valve dynamics has been modeled in an on-off modality, where the reconstructed leaflets opened and closed instantaneously according to the following rule [144]:

- if $\Delta P > 0 \rightarrow$ valve opens,

- if $Q_{AV} < 0 \rightarrow$ AV closes,
- if $Q_{MV} < 0$ & $t > 0.77$ s $\rightarrow$ MV closes,

where ΔP is the difference between upstream and downstream pressures and Q_{AV} and Q_{MV} are the flow rates through AV and MV, respectively. Moreover, in order to guarantee a perfect adhesion between the valves and LH internal wall surfaces, we imposed that both valves move in accordance with the ALE movement of LH.

Regarding the remaining boundary conditions of system (1), we prescribed a Neumann condition in the normal direction by imposing on Σ_{PV} a constant pressure of 10 mmHg for H [145, 146] and a time dependent evolution for R [106], see Figure 13C, whereas a time dependent physiological trend representing the aortic pressure [106,146] at Σ_{AR} for both cases, see Figure 13C. In the tangential direction, in order to avoid possible backflows instabilities, we prescribed a null velocity [147].

To numerically solve system (1), we used first-order Finite Elements together with fist order semi-implicit discretization in time [144]. The numerical scheme was stabilized by means of a Streamline Upwind Petrov-Galerkin/Pressure-Stabilizing Petrov-Galerkin (SUPG/PSPG) scheme [148] implemented in the multiphysics high performance library life^x [149] (https://lifex.gitlab.io/) based on the deal.II core [150]. We ran the simulations using 384 parallel processes on the GALILEO100 supercomputer (https://www.hpc.cineca.it/hardware/galileo100) at the CINECA high-performance computing center (Italy). Tetrahedral meshes were generated in VMTK with an average mesh element size equal to 1.1 mm for H and 1.5 mm for R, with a local refinement of 0.3 mm close to valves, corresponding to about 1.8M degrees of freedom in both the cases (see Figure 13B for the mesh of R). The timestep Δt was equal to $5 \cdot 10^{-4}$ s. We performed a mesh convergence test ensuring that no significant differences may be found by using a finer mesh or a smaller timestep.

We simulated 13 heartbeats and we discarded the first one to remove the influence of the null initial condition.

2.2.5 Quantities of interest

To describe and quantify the transition to turbulence, risk of hemolysis and thrombi formation in the two scenarios, we quantitatively analyzed and evaluated pressure and

velocity, solutions of (1). We referred to them as ensemble quantities, calculated over 12 heartbeats. Moreover, we calculated also other quantities obtained by a post-processing of the ensemble velocity:

- wall shear stresses (WSS), that is a function of space and time representing the viscous forces, per unit of area, exerted by the blood on the walls [151]. In particular, we computed the time average wall shear stresses, TAWSS(x). High values of TAWSS may damage the LH endocardium and trigger possible remodeling processes [152];
- relative residence time (RRT), that is a function of space measuring the total time a fluid particle spends on the LH internal wall surfaces. High values of this quantity may be a marker of stagnant flow [153];
- E-wave propagation index (EPI), that is the ratio between the space covered by the blood jet developing at the MV orifice during the E-wave and the length of the ventricle at the end diastolic configuration. Values of EPI < 1 could indicate an incomplete apical washout, leading to possible left ventricle thrombus formation [154];
- standard deviation (SD) at each time and space of the blood velocity with respect to its ensemble value. This allowed us to quantify and localize the regions characterized by marked transition to turbulence [140, 141];
- Global Turbulent Kinetic Energy (GTKE, known also as Integrated Fluctuating Kinetic Energy) at each time, quantifying the velocity fluctuations by means of the fluid Reynolds stress tensor [120, 155];
- maximum tangential stress τ_{max} of the fluid Reynolds stress tensor [155], that is a function of space and time quantifying the fluctuating (turbulent) forces exerted among the fluid layers and thus possible damage caused to blood cells. Notice that values greater than 800 Pa are considered to create the conditions that promote hemolysis [156].

2.3 Results

In Figure 14A, we reported the trend in time of the mean ensemble ventricular (LV), aortic (AR) and atrial (LA) pressures in the blue, red and magenta spheres, respectively. Notice that the maximum systolic drop ΔP_{AV} between LV and AR

pressures was reached at the middle of systole for H and slightly later (about 60 ms) for R, with values of 22 mmHg and 14 mmHg, respectively. As expected, R featured a lower ΔP_{AV} with respect to H, due to the presence of regurgitation [157]. The closure of the aortic valve occurred at 0.30 s for H (i.e. at 33% of the heartbeat) and at 0.32 s for R (i.e. at 40% of the heartbeat). During the diastolic phase, the ventricle pressure remained almost constant in H, with a peak of pressure drop between LA and LV ΔP_{MV} during the E-wave equal to 3.6 mmHg and 12.5 mmHg for H and R, respectively. The larger peak of ΔP_{MV} featured by R with respect to H was in accordance with [158]. The closure of the mitral valve occurred at 0.9 s and 0.8 s for H and R, respectively. Regarding the atrial pressure, in accordance to the boundary conditions imposed at PVs, we observed in the healthy case a constant value of 10 mmHg during the whole heartbeat, whereas, in the regurgitant scenario the pressure increased up to 40 mmHg. In Figure 14B, we reported the ensemble flow rates evaluated through AV (blue plane) and MV (red plane) for the two scenarios. During the systolic phase, the AV flow rate reached a maximum of 617 mL/s for H and 530 mL/s for R. Notice that the peak of the AV flow rate was reached at the same instant of maximum systolic ΔP_{AV} in both the scenarios. Moreover, the flow rate through MV in R featured a peak of 574 mL/s. During diastole, in the trend of MV flow rate we recognized the E-wave (first minimum), the A-wave (second minimum) and the diastasis (middle stage of diastole). The E-wave featured a maximum absolute value of 650 mL/s and 1525 mL/s for H and R, respectively. The higher diastolic MV flow rate in R was in accordance with [159]. During diastasis, the MV flow rate decelerated until a slightly reversal at 0.63 s (i.e. 70% of the heartbeat) and 0.60 s (i.e. 75% of the heartbeat) for H and R, respectively. During the A-wave, the flow rate reached absolute values of 190 mL/s for H and 392 mL/s for R. After the A-wave, the second flow reversal through MV occurred at 0.77 s (i.e. 96% of the heartbeat) in the regurgitant scenario.

In Figure 15, we reported the magnitude of the ensemble velocity field on a slice along the 3CH axis at three representative time instants: the instant of peak systole (i.e. maximum AV flow rate) t_{PS}, of peak E-wave t_{EW} , and of peak A-wave t_{AW}. In particular, t_{PS} = 0.15 s and 0.21 s, t_{EW} = 0.45 s and 0.465 s, t_{AW} = 0.8 s and 0.7 s, for H and R, respectively. At t_{PS} we displayed also a slice along the 2CH axis (see the black box), to better highlight that part of the ventricle flow went in the atrium resulting in

the formation of a regurgitant jet developing along the anterior leaflet and along the LA walls, with a velocity peak of 5.5 m/s at the level of the MV orifice. The maximum velocity through the AV plane was equal to 2.1 m/s for H and 1.5 m/s for R. As expected, the peak of AV velocity was higher in the healthy scenario [106, 124]. Notice also the different velocity distributions in the atrium in the two scenarios: in H, no specific velocity patterns were observed, whereas in R the regurgitation promoted chaotic and irregular structure formations. At t_{EW} when the blood flow went from LA to LV, we obtained maximum velocity values through MV equal to 1.08 m/s and 1.73 m/s for H and R, respectively, highlighting the more elevated velocity in R, due to the higher MV flow rate, see Figure 14B. Furthermore, in both the scenarios we observed the formation of a ventricular vortex ring developing below the anterior leaflet. Moreover, during the E-wave we calculated the value of EPI in the ventricle, which was equal to 1 and 2 for H and R, respectively, highlighting the better ability of R to washout ventricular blood than H. At t_{AW} the second injection of fluid in the ventricle occurred. The velocity through MV were lower with respect to the ones observed at t_{EW} for both the scenarios. Furthermore, we noticed swirling structures in the ventricle, especially in correspondence of the middle-apex areas, due to vortices formed during the diastasis.

In Figure 16, we reported the volume rendering of the ensemble velocity magnitude at t_{PS} (panel A), the spatial distribution of TAWSS (panel B) and RRT (panel C) for the two scenarios, in two different views. From this figure we observed that for R the regurgitant jet gave rise to high velocities, elevated values of TAWSS, and low values of RRT where the blood flow scratched and impinged against the atrial walls. Notice also that in the ventricle, TAWSS was slightly higher in R due to larger velocities occurred during the diastolic phase, see Figure 15. To quantify these differences, we reported in Table 3, the percentage of area with RRT greater than 5 Pa^{-1}, computed over the total LV surface, the LV apex, the total LA surface, and left atrial appendage (LAA), in the two scenarios. Notice that such values were in any case larger for H than R. We pointed out that this threshold was chosen as representative value to discriminate high and low values of RRT. However, the analysis performed with other thresholds led to the same conclusions (percentage of area above the threshold larger in H).

In Figure 17A, we reported, for each scenario, the evolution in time of GTKE evaluated in LV and LA. We observed that in R GTKE was much larger than in H in all the two chambers, with maximum values in LA at the end of systole due to the regurgitant jet and almost constant values in LV. With t_{GTKE} we referred to the time instant of maximum GTKE, equal to 0.29 s (i.e. at 32% of the heartbeat) and to 0.25 s (i.e. at 31% of the heartbeat) for H and R, respectively. In Table 3, we reported the average in time of GTKE, for both the scenarios confirming larger values for R. In Figure 17B, we displayed at t_{GTKE} and t_{EW} two slices along the 2CH (left) and 3CH (right) axes with the velocity SD. R featured in any case larger values of SD in all the left heart than H, confirming the greater predisposition of R to develop transition to turbulence. SD values in R at t_{GTKE} were comparable with the ensemble velocity ones, with a peak of 183 cm/s in correspondence of the regurgitant jet and of 39 cm/s in LV. Instead in H, the maximum SD value was equal to 17 cm/s in LA and to 19 cm/s in LV. Notice also a peak of 31 cm/s located in AR. At t_{EW}, the fluctuations were mainly present in the center of LA with a peak of 55 cm/s in R. Instead in H, we noticed very low SD values with a peak in the LA center of 13 cm/s.

In Figure 18A, we reported for the regurgitant scenario the volume rendering of τmax at the instants where the volume of blood characterized by τmax > 800 Pa featured its peaks, $t_1 = 0.07$ s and $t_2 = 0.24$ s, see Figure 18B. We observed values of τ_{max} greater than 800 Pa when the regurgitant jet impinged against the atrial walls (t1) and when a rapid deceleration of the regurgitant flow through MV occurred (t2), see also Figure 14B. From Figure 18B, we observed that during the diastolic phase the volume with elevated τ_{max} was always null. We also computed the total exposure time to values greater than 800 Pa, which was equal to 220 ms for R and 0 ms for H, suggesting the absence of hemolysis in the healthy scenario (see Table 3).

In Figure 13A, we reported, for the healthy scenario, the three locations of the acquisitions of ECD peak velocity measures. In particular, to assess the accuracy of the results of subject H reported in this work we compared the velocity field computed by the numerical simulation with such measures. In Table 4, we reported the corresponding values in the three locations. The maximum relative error Δ was found in P2 (5.9%), whereas in P1 and P3 the error was no larger than 4.0%.

In Figure 19, we reported a qualitative comparison of the regurgitant flow pattern obtained by the numerical simulation (bottom) with cine-MRI (top) at the three representative frames in R. In particular, in the cine-MRI views the regurgitant jet was detected by the areas characterized by a darker color, representing high blood flow velocities. Notice the good qualitative agreement between computations and images, highlighting that the regurgitant jet firstly developed along the anterior leaflet (Frames 1 and 2) and then also along the atrial walls assuming also a swirling structure (Frame 3).

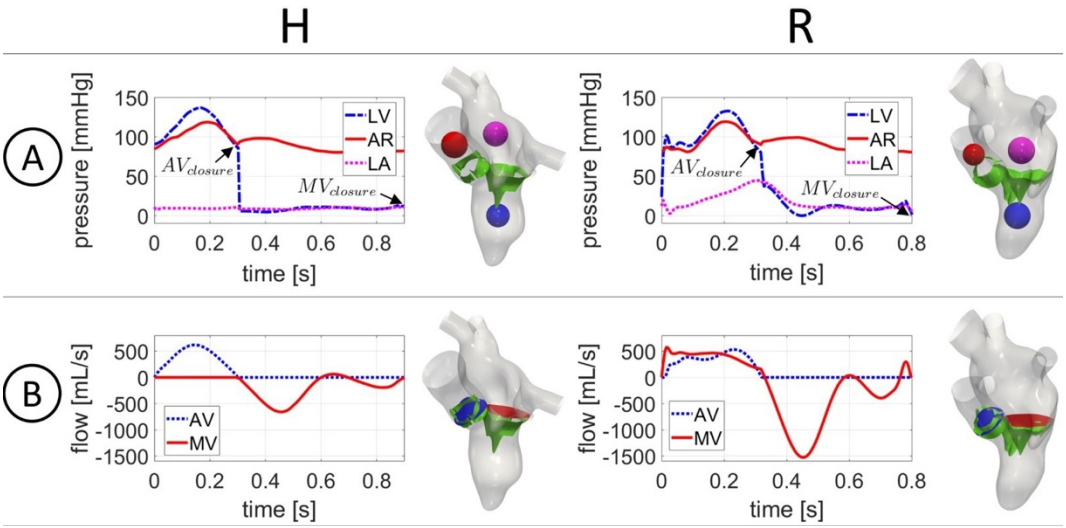

Fig. 14 For each scenario: A: trend in time of the mean ensemble ventricle (LV), aortic (AR) and atrial (LA) pressures in the blue, red and magenta spheres, respectively; B: trend in time of the ensemble flow rates through AV (blue section) and MV (red section). $AV_{closure}$: closure of aortic valve; $MV_{closure}$: closure of mitral valve.

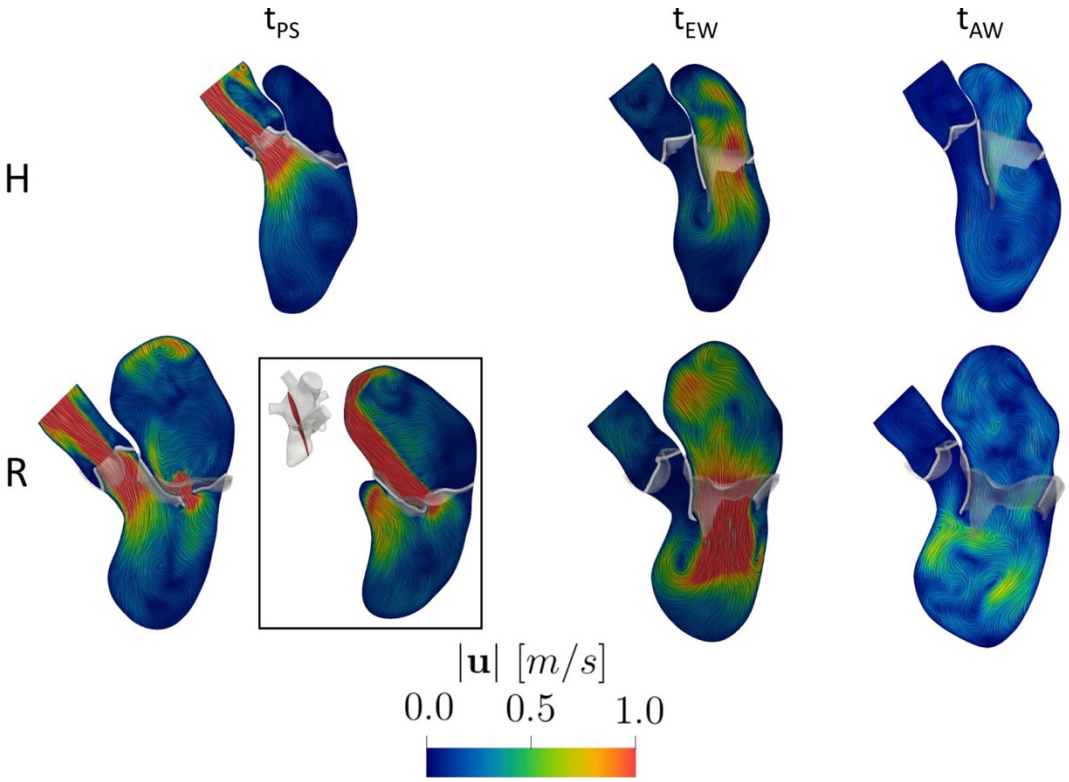

Fig. 15 Magnitude of the ensemble velocity at three representative time instants over a slice along the 3CH axis in the two scenarios. At t_{PS}, we also reported a slice along the 2CH axis (black box) for the regurgitant case.

Scenario	*EPI* [–]	*AREA RRT* $> 5\ Pa^{-1}$ [%]				$\overline{GTKE}$ [*mJ*]		*t* $\tau_{max} > 800\ Pa$ [*ms*]
		LV	LV_{apex}	LA	LAA	LV	LA	
H	1	68	83	48	100	0.20	0.12	0
R	2	40	53	33	100	4.80	7.30	220

Table 3 Values of the quantities of interest computed for each scenario. EPI: E-wave propagation index; Percentage of area with RRT greater then $5\ Pa^{-1}$ evaluate in four different locations LV, *LVapex*, LA, and LAA); *GTKE*: average in time of GTKE evaluated in LV and LA; Total exposure time of the blood to values of $\tau_{max} > 800\ Pa$.

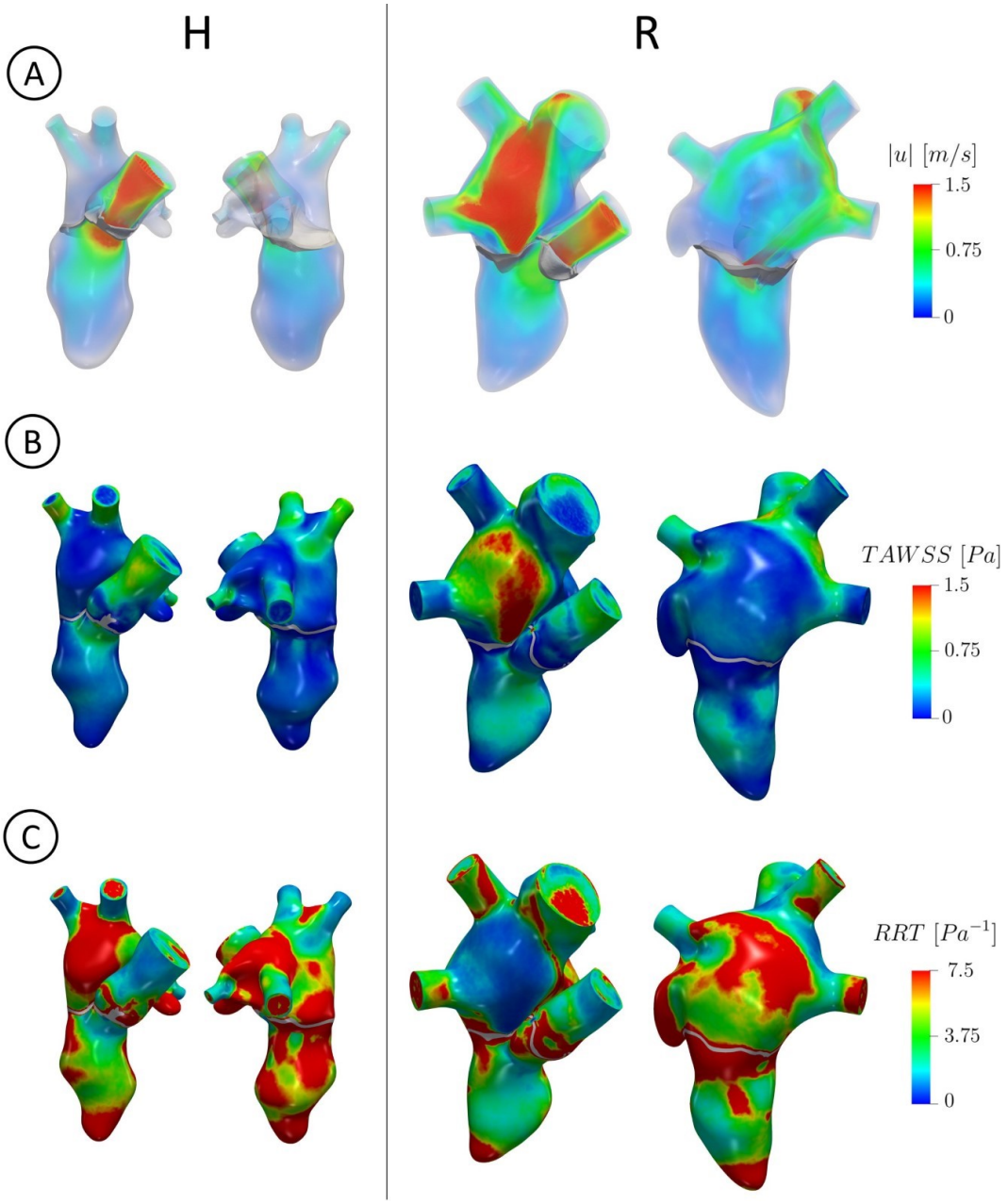

Fig. 16 For each scenario in two different views: A: volume rendering of the ensemble velocity magnitude at t_{PS}; B: spatial distribution of TAWSS, reported in the end systolic configuration; C: spatial distribution of RRT, reported in the end systolic configuration.

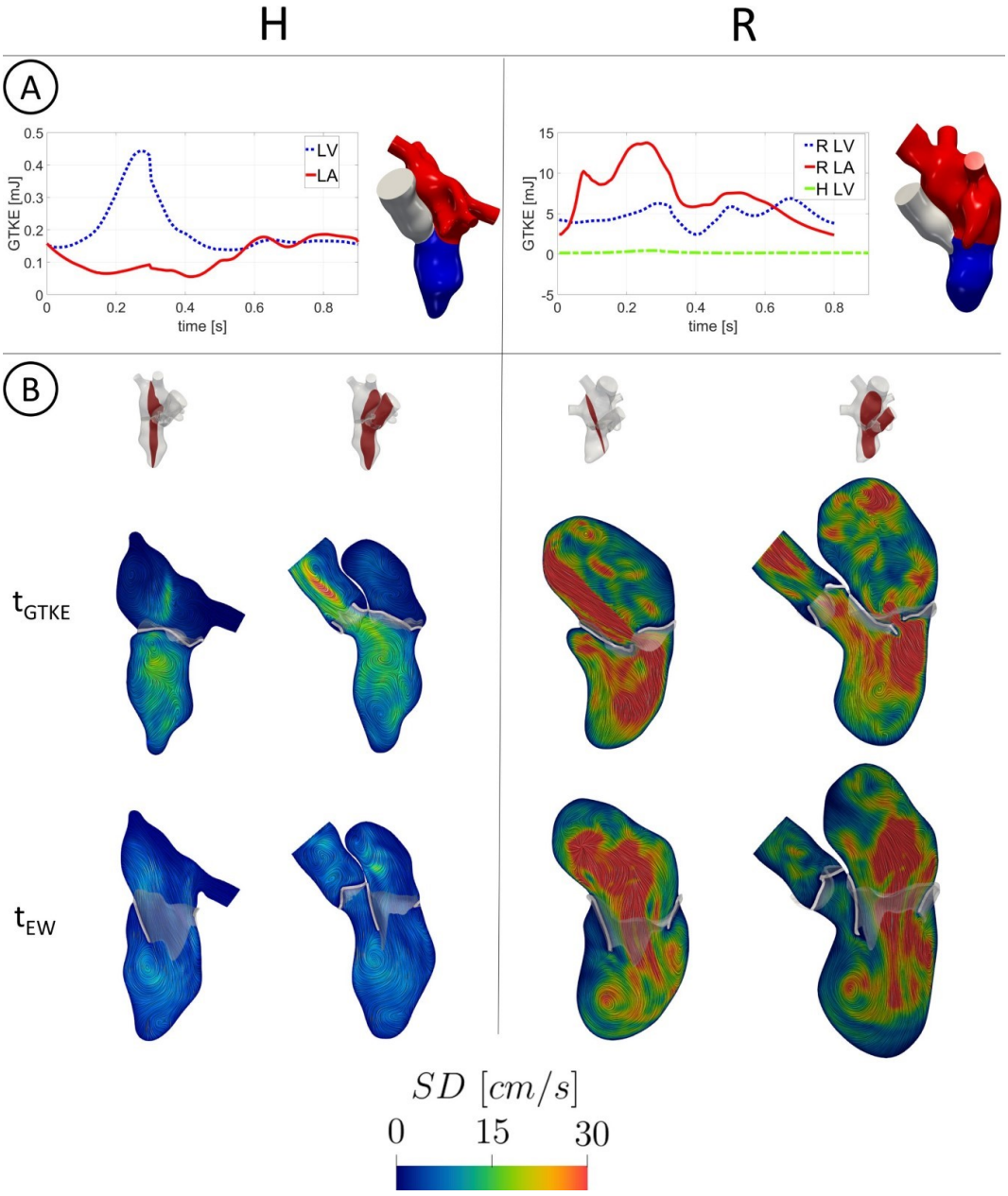

Fig. 17 A: trend in time of GTKE evaluated in LV and LA. Notice the different scale used for H (left) and R (right). In the right figure, also the H LV case has been reported for a direct comparison; B: slices along the 2CH (left) and 3CH (right) axis with the velocity SD at $t_{GT\ KE}$ and t_{EW} .

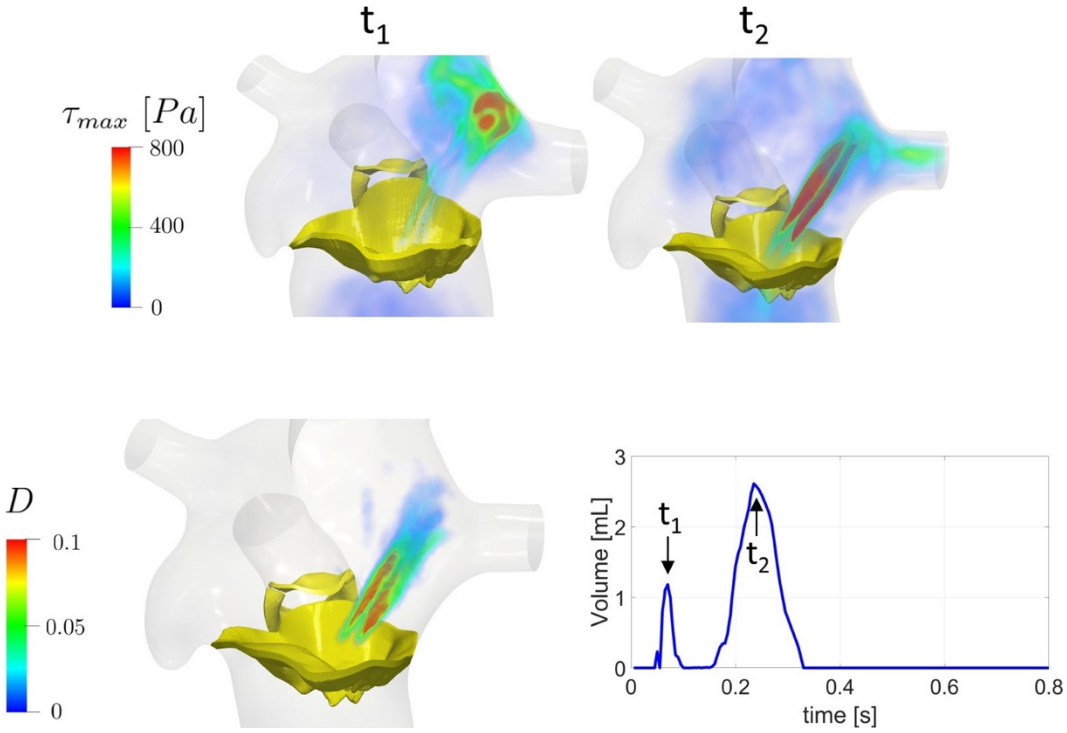

Fig. 18 Top: volume rendering at two different time instants t_1 and t_2 of the maximum tangential stress τ_{max} quantifying the possible damage caused to blood cells in the regurgitant scenario; Bottom, left: Percentage $D(\mathbf{x})$ of the cardiac cycle duration during which $\tau max >$ 800 Pa; Bottom, right: time evolution of the volume of blood characterized by $\tau_{max} >$ 800 Pa and identification of t_1 and t_2 as the peak instants.

	P1			P2			P3		
Scenario	*ECD* $[m/s]$	*SIM* $[m/s]$	Δ [%]	*ECD* $[m/s]$	*SIM* $[m/s]$	Δ [%]	*ECD* $[m/s]$	*SIM* $[m/s]$	Δ [%]
H	1.25	1.20	4.0	0.85	0.80	5.9	0.62	0.60	3.2

Table 4. Comparison for the healthy case between the measurement of ECD and the values of the numerical simulation (SIM) in the three points of Figure 2A. Δ is the relative discrepancy.

2.4 Discussion

In this work we performed an image-based computational fluid dynamic study in the left heart of a healthy subject and of a patient with a severe MVR, with the aim of comparing the transition to turbulence, the risk of hemolysis, and the risk of thrombi formation. The motion of the complete LH (LV, LA, and AR internal wall surfaces, together with AV and MV) during the whole heartbeat was reconstructed and prescribed to DIB-CFD simulations from cine-MRI images.

At the best of our knowledge, this is the first work using all the patient-specific geometry motion of LV, LA, AR, AV and MV surfaces in a DIB-CFD simulation. In particular, for the healthy case the majority of the previous DIB-CFD studies did not include LA or AR or employed template geometries [105, 116, 121, 122, 124, 125]. In [109, 117, 120] the authors reconstructed all the patient-specific LH walls of a healthy subject, where however MV and AV in [109] and AV in [117, 120] were geometrically modeled as planes in their FC configuration and disappeared in the FO configuration. For the regurgitant case, no patient-specific LA and MV motions could be found in previous studies.

In our work, we included both the valves and the entire reconstruction of the LH internal wall surfaces and valves was performed by combining different acquisitions of cine-MRI images at disposal: the LV Long Axis, the LV Short Axis, the AR Short Axis (when available) and the MV Rotated series. The latter stand out from the other series because they are based on a radial sampling (while the other series on a Cartesian sampling) which consist in 2D Long Axis series of 18 evenly rotated planes (one every 10 degree) around the axis passing through the MV center and aligned with the LV apex, proposed for the first time in [128] for a pure structural analysis. Such images represented advanced acquisitions not acquired in the clinical routine, see Figure 1, which allowed us to obtain detailed 3D geometry motion of LA, AR, MV and AV, in addition to ventricle motion for which the LV Short and Long Axis series are sufficient.

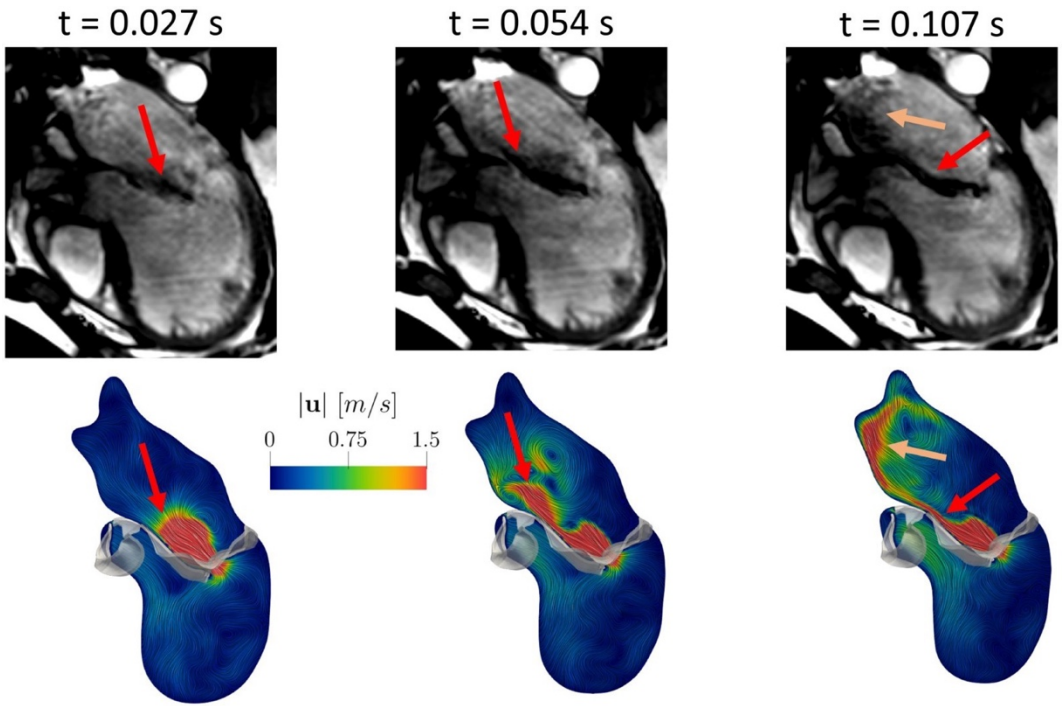

Fig. 19 Comparison of the ensemble velocity pattern with Cine-MR images at three representative frames in the regurgitant scenario. The arrows highlight the good agreement between computations and measures.

Owing to this specific and detailed imaging, we were able to quantitatively describe physiological and pathological/MVR mechanisms such as prevention from thrombi, transition to turbulence, and hemolysis formation. In particular, for the first time at the best of our knowledge, we investigated by means of a computational study how the regurgitant jet could promote the washing out of regions with stagnant flow in LA, reducing the risk of thrombosis with respect to a healthy scenario. Our results highlighted that the regurgitant jet scratched against the atrial walls, see Figure 5A, resulting in elevated values of TAWSS, see Figure 5B. This led to low values of RRT (Figure 5C) indicating that there is little stagnation in those regions and thus promoting the washing out of blood. This was also confirmed by the values reported in Table 2. Notice however that RRT in LAA was elevated in both the subjects, confirming that, even in MVR, LAA could be one of most common site for cardiac thrombus formation [70]. Moreover, we investigated the mechanism of washing out occurring in the ventricle during the E-wave. In particular, in the regurgitant scenario there was a

significant LV apical washout due to high blood flow coming from MV, see Figs. 3B and 4 as confirmed by the value of EPI and of low RRT areas, see Table 2. The high velocities through MV allowed the blood to reach the ventricle apex rapidly and with high energy before diastasis, allowing to remove possible areas of stagnant flow [154]. Thus, MVR promoted a more relevant washout, with respect to the physiological case, of the blood flow in LA during the systolic phase and in LV during the E-wave, leading to regions more protected from the possible formation of clots. Such results are in agreement with clinical studies [104, 161, 162]. Second, we investigated the transition to turbulence in the MVR case. So far, at the best of our knowledge, the turbulent effects were investigated only in physiological LH [117, 120]. By employing a LES model, we showed that the regurgitant scenario featured high velocity fluctuations among the heartbeats, resulting in elevated velocity standard deviation, see Figure 6 and the values of GTKE reported in Table 2. In particular, the maximum fluctuations in LA occurred for R at late systole, as also reported in [102], with a GTKE peak value equal to 14 mJ, which falls in the range (103,127) mJ found in [102]. Moreover, the ratio of the average GTKE in LA between R and H was equal to 61, see Table 2, confirming that the presence of the regurgitant jet promoted more turbulence in R. We noticed also elevated transition to turbulence for R in LV, especially during the rapid deceleration of the systolic blood flow (Figure 3B), during the E-wave due to the formation of a ventricular vortex ring and to the impingement of the diastolic jet against the LV apex (Figure 4), and during the A-Wave due to the mixing of blood after diastasis (Figure 4). The ratio of the average GTKE in LV between R and H was equal to 24, highlighting how the regurgitation promoted a great amount of turbulence also in LV. We point out that the transition to turbulence in LV was more pronounced for R because of the larger heart dimension resulting in higher ventricular blood flow. Since the BSA of the two subjects was very similar (see Table 2), we argue that the larger LH dimensions of patient R were due uniquely to MVR, which is known to be correlated with progressive remodeling and dilation [73]. In this respect, we noticed that the ratio between R and H LV diameters at the end diastolic configuration was equal to 1.25, a value in agreement with medical studies reporting that severe MVR dilated the left ventricle diameter by a factor of 25-30% [164, 165].

Third, we observed that the definition of τ_{max} (see Section "Quantities of interest") implies that large transition to turbulence (and thus large values of $\tau_{max)}$ promotes hemolysis. In particular, we found high values of τ_{max} (greater than 800 Pa, identified as a risk threshold [156]) in correspondence of the regurgitant jet, see Figure 7A. We highlighted two different mechanisms (Figure 7B) that provoke large τ_{max}: at t_1 the fragmentation of the regurgitant jet against the atrial walls; at t_2 the rapid deceleration of the blood flow through MV, see also Figure 3B. These two different mechanisms were also described by clinical studies [103,166]. Furthermore, according to [156], regions exposed to value of τmax larger than 800 Pa for more than 1 ms could experience the conditions of promoting hemolysis. In our R case, we found a value of 220 ms, see Figure 7B, and Table 3.

The blood velocity results found in this work for the healthy case have been validated against ECD measures acquired in the subject in three different locations. In particular, although far to establish a complete validation, they are very promising since they highlighted a good accuracy (with a maximum error of 6%, see Table 4) between the maximum values. Furthermore, we reported a qualitative comparison of the regurgitant flow pattern obtained by the numerical simulation with the cine-MRI, see Figure 8. We noticed a good agreement between the cine-MRI images and the numerical simulations. In particular, the direction of the regurgitant jet in the numerical simulation was also in accordance with the Carpentier's functional classification for which, in case of MVR due to a prolapse, the jet is directed away from the pathological leaflet, in our case the posterior one [167, 168]. To support the other results and the physio-pathological implications, we compared our findings with the literature. In particular, in the healthy scenario the value of the maximum pressure drop $\Delta P_{MV} = 3.6$ mmHg computed across MV falls down in the same range $\simeq$ (2.0,4.0) mmHg found in [169]. In the regurgitant scenario, we compared our velocity findings with measures in the case of a severe MVR. We found a value of the maximum velocity through MV at systole equal to 5.52 m/s, in accordance with the range (5.00,6.00) m/s [102], and during the E-Wave equal to 1.73 m/s, in accordance with the range (1.18,1.77) m/s [170]. Notice that the E-Wave peak velocity value is used in clinics to assess the severity of MVR. Notice also that the MV flow reversals detected at diastasis ($t \simeq 0.59$

s) and before the end of the heartbeat ($t \simeq 0.77$ s, see Figure 3B) were also found in other computational studies [106, 109, 171].

2.5 Limitations

Some limitations characterized this work:

1. We considered only two subjects. This was a consequence of the fact that we used advanced (not daily available) images series elaborated in order to perform highly accurate DIB-CFD simulations. This allowed us to extract interesting general physio-pathological findings of the healthy and regurgitant scenarios. As a consequence, our reconstruction technique is not suitable to study a wide range of specific subjects, for which standard images are enough;
2. We did not model the valve dynamics, instead we considered a instantaneous valve opening and closure. However, the opening and closing valve time duration is less than 5% of the heartbeat [82]. Thus, the opening and closure of the valves can be considered as instantaneous as a first approximation. The degree to which a patient-specific valve dynamics may affect the velocity field and the transition to turbulence is currently under study;
3. We did not include the subvalvular apparatus (papillary muscles + chordae tendineae) in the LV geometry. This is a common choice, adopted also in [116, 118, 119, 121, 122] due to the difficulty to reconstruct the papillary muscles and chordae tendineae from MRI images. However, their influence on the quantities of interest, in particular on transition to turbulence, should be relevant and it will be the subject of future studies;
4. We did not considered the MRI beat-to-beat variations in terms of acquired displacements and heart rate. Indeed, the average of MRI acquisitions along more heartbeats should provide more reliable input data for DIB-CFD. However, this may result in prolonged exposure time during the acquisitions of cine-MRI, that is not advisable for patients with heart pathologies.

3. Conclusion

Computational fluid dynamic with prescribed wall motion and immersed mitral valve revealed to be an effective tool to quantitatively describe hemodynamics in case of MVR and to compare different regurgitant scenarios. Our findings highlighted in particular the presence of transition to turbulence in the atrium and allowed us to quantify some important cardiac indices such as cardiac output and WSS.

Our results also highlighted that the regurgitant jet in the mitral valve regurgitation case gave rise to a large amount of transition to turbulence in the left atrium resulting in a higher risk of formation of hemolysis. Moreover, mitral valve regurgitation promoted a more complete washout of stagnant flows in the left atrium during the systolic phase and in the left ventricle apex during diastole.

Although we acknowledge that further work and analysis will be needed, this new method to approach the study of mitral valve may develop in a novel tool able to perform a fine analysis of the mitral valve pathophysiology and the comparison of different surgical techniques of the diseased mitral valve undergone a surgical repair.

4. References

1. Harb, S.L., Griffin, B.P.: Mitral valve disease: a comprehensive review. Curr Cardiol Rep. **19**(73) (2017). https://doi.org/10.1007/ s11886-017-0883-5

2. Wu, S., Chai, A., Arimie, S., Mehra, A., Clavijo, L., Matthews, R., Shavelle, D.: Incidence and treatment of severe primary mitral regurgita- tion in contemporary clinical practice. Cardiovascular Revascularization Medicine **19** (2018). https://doi.org/10.1016/j.carrev.2018.07.021

3. Kon, M., Myerson, S., Moat, N., Pennell, D.: Quantification of regurgitant fraction in mitral regurgitation by cardiovascular magnetic resonance: Comparison of techniques. The Journal of heart valve disease **13**, 600–7 (2004).

4. Falk, V., Seeburger, J., Czesla, M., Borger, M.A., Willige, J., Kuntze, T., Doll, N., Borger, F., Perrier, P., Mohr, F.W.: How does the use of poly- tetrafluoroethylene neochordae for posterior mitral valve prolapse (loop technique) compare with leaflet resection? A prospective randomized trial. The Journal of Thoracic and Cardiovascular Surgery **1200-1206**, 600–7 (2008). https://doi.org/10.1016/j.jtcvs.2008.07.028

5. Pfannmueller, B., Misfeld, M., Verevkin, A., Garbade, J., Holzhey, D.M., Davierwala, P., Seeburger, J., Noack, T., Borger, M.A.: Loop neochord versus leaflet resection techniques for minimally invasive mitral valve repair: long-term results. European Journal of Cardio-Thoracic Surgery **59**(1), 180–186 (2020). https://doi.org/10.1093/ejcts/ezaa255 v

6. Gao, H., Qi, N., Feng, L., Ma, X., Danton, M., Berry, C., Luo, X.: Mod- elling mitral valvular dynamics - current trend and future directions: Review of mv modelling. International Journal for Numerical Methods in Biomedical Engineering **33** (2016). https://doi.org/10.1002/cnm.2858 v

7. Fumagalli, I., Fedele, M., Vergara, C., Dede', L., Ippolito, S., Nicol`o, F., Antona, C., Scrofani, R., Quarteroni, A.: An image-based computational hemodynamics study of the systolic anterior motion of the mitral valve. Computers in Biology and Medicine **123**, 103922 (2020). https://doi.org/ 10.1016/j.compbiomed.2020.103922

8. Mittal, R., Seo, J.H., Vedula, V., Choi, Y., Liu, H., Huang, H., Jain, S., Younes, L., Abraham, T., George, R.: Computational modeling of cardiac hemodynamics: Current status and future outlook. Journal of Computational Physics **305** (2015). https://doi.org/10.1016/j.jcp.2015. 11.022

9. McQueen, D.M., Peskin, C.S., Yellin, E.L.: Fluid dynamics of the mitral valve: physiological aspects of a mathematical model. American Journal of Physiology-Heart and

Circulatory Physiology **242**(6), 1095–1110 (1982). https://doi.org/10.1152/ajpheart.1982.242.6.H1095

10. Kunzelman, K.S., Einstein, D.R., Cochran, R.P.: Fluid structure interac- tion models of the mitral valve: function in normal and pathological states. Philosophical Transactions of the Royal Society B: Biological Sciences **362**(1484), 1393–1406 (2007). https://doi.org/10.1098/rstb.2007.2123

11. Ma, X., Gao, H., Griffith, B., Berry, C., Luo, X.: Image-based fluid- structure interaction model of the human mitral valve. Computers and Fluids **71**, 417–425 (2013). https://doi.org/10.1016/j.compfluid.2012.10. 025

12. Su, B., Zhong, L., Wang, X.-K., Zhang, J.-M., Tan, R.S., Allen, J.C., Tan, S.K., Kim, S., Leo, H.L.: Numerical simulation of patient-specific left ventricular model with both mitral and aortic valves by FSI approach. Computer Methods and Programs in Biomedicine **113**(2), 474–482 (2014). https://doi.org/10.1016/j.cmpb.2013.11.009

13. Gao, H., Qi, N., Ma, X., Griffith, B., Berry, C., Luo, X.: Fluid-structure interaction model of human mitral valve within left ventricle, pp. 330–337 (2015). https://doi.org/10.1007/978-3-319-20309-6 38

14. Gao, H., Feng, L., Qi, N., Berry, C., Griffith, B.E., Luo, X.: A coupled mitral valve-left ventricle model with fluid–structure interaction. Medi- cal Engineering Physics **47**, 128–136 (2017). https://doi.org/10.1016/j. medengphy.2017.06.042

15. Feng, L., Gao, H., Griffith, B., Niederer, S., Luo, X.: Analysis of a cou- pled fluid-structure interaction model of the left atrium and mitral valve. International Journal for Numerical Methods in Biomedical Engineering **35**(11) (2019). https://doi.org/10.1002/cnm.3254

16. Caballero, A., Mao, W., McKay, R., Sun, W.: Transapical mitral valve repair with neochordae implantation: FSI analysis of neochordae number and complexity of leaflet prolapse. International Journal for Numerical Methods in Biomedical Engineering **36**(3), 3297 (2020). https://doi.org/ 10.1002/cnm.3297

17. Lassila, T., Malossi, A.C.I., Stevanella, M., Votta, E., Redaelli, A., Deparis, S.: Simulation of left ventricle fluid dynamics with mitral regur- gitation from magnetic resonance images with fictitious elastic structure regularization (2017). https://doi.org/10.48550/arXiv.1707.03998

18. Caballero, A., Mao, W., McKay, R., Primiano, C., Hashim, S., Sun, W.: New insights into mitral heart valve prolapse after chordae rupture through fluid–structure interaction computational modeling. Scientific Reports **8** (2018). https://doi.org/10.1038/s41598-018-35555-5

19. Peskin, C.S.: The immersed boundary method. Acta Numerica **11**, 479– 517 (2002). https://doi.org/10.1017/S0962492902000077

20. Bavo, A., Pouch, A., Degroote, J., Vierendeels, J., Gorman III, J., Gor- man, R., Segers, P.: Patient-specific CFD simulation of intraventricular haemodynamics based on 3D ultrasound imaging. Biomedical engineering online **15** (2016). https://doi.org/10.1186/s12938-016-0231-9

21. Bavo, A., Pouch, A., Degroote, J., Vierendeels, J., Gorman III, J., Gor- man, R., Segers, P.: Patient-specific CFD models for intraventricular flow analysis from 3D ultrasound imaging: Comparison of three clinical cases. Journal of Biomechanics **50** (2016). https://doi.org/10.1016/j.jbiomech. 2016.11.039

22. Vellguth, K., Bru¨ning, J., Goubergrits, L., Tautz, L., Hennemuth, A., Kertzscher, U., Degener, F., Kelm, M., Su¨ndermann, S., Kuehne, T.: Development of a modeling pipeline for the prediction of hemodynamic outcome after virtual mitral valve repair using image-based CFD. Inter- national Journal of Computer Assisted Radiology and Surgery **13** (2018). https://doi.org/10.1007/s11548-018-1821-8

23. Su, B., Tan, R.S., Tan, J.L., Guo, K.W.Q., Zhang, J.M., Leng, S., Zhao, X., Allen, J.C., Zhong, L.: Cardiac MRI based numerical modeling of left ventricular fluid dynamics with mitral valve incorporated. Jour- nal of Biomechanics **49**(7), 1199–1205 (2016). https://doi.org/10.1016/j. jbiomech.2016.03.008

24. Fumagalli, I., Vitullo, P., Vergara, C., Fedele, M., Corno, A.F., Ippolito, S., Scrofani, R., Quarteroni, A.: Image-based computational hemody- namics analysis of systolic obstruction in hypertrophic cardiomyopathy. Frontiers in Physiology **12** (2022). https://doi.org/10.3389/fphys.2021. 787082

25. Collia, D., Zovatto, L., Pedrizzetti, G.: Analysis of mitral valve regurgita- tion by computational fluid dynamics. APL Bioengineering **3**(3), 036105 (2019). https://doi.org/10.1063/1.5097245

26. Obermeier, L., Vellguth, K., Schlief, A., Tautz, L., Bru¨ning, J., Knosalla, C., Kuehne, T., Solowjowa, N., Goubergrits, L.: Ct-based simulation of left ventricular hemodynamics: A pilot study in mitral regurgitation and left ventricle aneurysm patients. Frontiers in Cardiovascular Medicine **9**, 828556 (2022). https://doi.org/10.3389/fcvm.2022.828556

27. Stevanella, M., Maffessanti, F., Conti, C., Votta, E., Arnoldi, A., Lom- bardi, M., Parodi, O., Caiani, E., Redaelli, A.: Mitral valve patient-specific finite element modeling from cardiac MRI: Application to an annuloplasty procedure. Cardiovascular Engineering and Technology **2**, 66–76 (2011). https://doi.org/10.1007/s13239-010-0032-4

28. Gaasch, W.H., Meyer, T.E.: Left ventricular response to mitral regurgi- tation. Circulation **118**(22), 2298–2303 (2008). https://doi.org/10.1161/CIRCULATIONAHA.107.755942

29. Bach, D.S., Deeb, G.M., Bolling, S.F.: Accuracy of intraoperative trans- esophageal echocardiography for estimating the severity of functional mitral regurgitation. The American journal of cardiology **76**(7), 508–512 (1995). https://doi.org/10.1016/s0002-9149(99)80140-4

30. Koelling, T., Aaronson, K., Cody, R., Bach, D., Armstrong, W.: Prog- nostic significance of mitral regurgitation and tricuspid regurgitation in patients with left ventricular systolic dysfunction. American heart journal **144**, 524–9 (2002). https://doi.org/10.1067/mhj.2002.123575

31. Pase, G.: An image-based computational hemodynamic study of hypertrophic cardiomyopathy. Master's thesis dissertation, Universit`a degli Studi di Trento (2020). https://www.biblioteca.unitn.it/282/tesi-di- laurea

32. Fetzer, A., Zelzer, S., Schroeder, T., Meinzer, H.-P., Nolden, M.: An interactive 3D segmentation for the Medical Imaging Interaction Toolkit (MITK). (2014). https://doi.org/10.13140/2.1.4169.6326

33. Wolf, I., Vetter, M., Wegner, I., B¨ottger, T., Nolden, M., Sch¨obinger, M., Hastenteufel, M., Kunert, T., Meinzer, H.-P.: The medical imaging interaction toolkit. Medical Image Analysis **9**(6), 594–604 (2005). https: //doi.org/10.1016/j.media.2005.04.005.

34. Nolden, M., Zelzer, S., Seitel, A., Nabers, D., Mu¨ller, M., Franz, A., Maleike, D., Fangerau, M., Baumhauer, M., Maier-Hein, L., Maier-Hein, K., Meinzer, H.-P., Wolf, I.: The medical imaging interaction toolkit: chal- lenges and advances. International journal of computer assisted radiology and surgery **8** (2013). https://doi.org/10.1007/s11548-013-0840-8

35. Antiga, L., Piccinelli, M., Botti, L., Ene-Iordache, B., Remuzzi, A., Stein- man, D.A.: An image-based modeling framework for patient-specific com- putational hemodynamics. Medical & biological engineering & computing **46**(11), 1097–1112 (2008). https://doi.org/10.1007/s11517-008-0420-1

36. Fedele, M., Quarteroni, A.: Polygonal surface processing and mesh generation tools for the numerical simulation of the cardiac function. International Journal for Numerical Methods in Biomedical Engineering **37** (2021). https://doi.org/10.1002/cnm.3435

37. Klein, S., Staring, M., Murphy, K., Viergever, M.A., Pluim, J.P.W.: Elastix: A toolbox for intensity-based medical image registration. IEEE Transactions on Medical Imaging **29**(1), 196–205 (2010). https://doi.org/ 10.1109/TMI.2009.2035616

38. Quarteroni, A., Sacco, R., Saleri, F.: Numerical Mathematics vol. 37, (2007). https://doi.org/10.1007/b98885

39. Quarteroni, A.: Numerical Models for Differential Problems vol. 2, (2013). https://doi.org/10.1007/978-88-470-1071-0

40. Chandraratna, P.A., Aronow, W.S.: Mitral valve ring in normal vs dilated left ventricle. cross-sectional echocardiographic study. Chest **79**(2), 151– 154 (1981). https://doi.org/10.1378/chest.79.2.151

41. Ballester, M., Jajoo, J., Rees, S., Rickardsm, A., Mcdonald, L.: The mech- anism of mitral regurgitation in dilated left ventricle. Clinical Cardiology **6**(7), 333–338 (1983). https://doi.org/10.1002/clc.4960060706

42. Brown, O.R., DeMots, H., Kloster, F.E., Roberts, A., Menashe, V.D., Beals, R.K.: Aortic root dilatation and mitral valve prolapse in marfan's syndrome: an ECHOCARDIOgraphic study. Circulation **52**(4), 651–657. (1975) https://doi.org/10.1161/01.CIR.52.4.651

43. Matos-Souza, J.R., Fernandes-Santos, M.E., Hoehne, E.L., Franchini, K.G., Nadruz, J. Wilson: Isolated mitral valve prolapse is an independent predictor of aortic root size in a general population. European Jour- nal of Echocardiography **11**(3), 302–305 (2009). https://doi.org/10.1093/ ejechocard/jep219

44. Watanabe, N., Maltais, S., Nishino, S., O'Donoghue, T.A., Hung, J.: Functional mitral regurgitation: Imaging insights, clinical outcomes and surgical principles. Progress in Cardiovascular Diseases **60**(3), 351–360 (2017). https://doi.org/10.1016/j.pcad.2017.11.006

45. Osteresch, R., Diehl, K., Dierks, P., Schmucker, J., Ammar, A., Marin, L., Fach, A., Frerker, C., Eitel, I., Hambrecht, R., Wienbergen, H.: Influence of the ratio of mean arterial pressure to right atrial pressure on outcome after successful percutaneous edge-to-edge repair for severe mitral valve regurgitation. IJC Heart & Vasculature **37**, 100903 (2021). https://doi.org/10.1016/j.ijcha.2021.100903

46. Shah, P.M.: Current concepts in mitral valve prolapse—diagnosis and management. Journal of Cardiology **56**(2), 125–133 (2010). https://doi. org/10.1016/j.jjcc.2010.06.004

47. Hirt, C.W., Amsden, A.A., Cook, J.L.: An arbitrary Lagrangian-Eulerian computing method for all flow speeds. Journal of Computational Physics **14**(3), 227–253 (1974). https://doi.org/10.1016/0021-9991(74)90051-5

48. Donea, J., Giuliani, S., Halleux, J.P.: An arbitrary Lagrangian-Eulerian finite element method for transient dynamic fluid-structure interactions. Computer Methods in Applied Mechanics and Engineering **33**(1), 689–723 (1982). https://doi.org/10.1016/0045-7825(82)90128-1

49. Stein, K., Tezduyar, T., Benney, R.: Mesh moving techniques for fluid- structure interactions with large displacements. Journal of Applied Mechanics **70**(1), 58–63 (2003). https://doi.org/10.1115/1.1530635

50. Fern´andez, Miguel A., Gerbeau, Jean-Fr´ed´eric, Martin, Vincent: Numer- ical simulation of blood flows through a porous interface. ESAIM: M2AN **42**(6), 961–990 (2008). https://doi.org/10.1051/m2an:2008031

51. Astorino, M., Hamers, J., Shadden, S.C., Gerbeau, J.-F.: A robust and efficient valve model based on resistive immersed surfaces. International Journal for Numerical Methods in Biomedical Engineering **28**(9), 937–959 (2012). https://doi.org/10.1002/cnm.2474

52. Fedele, M., Faggiano, E., Dede, L., Quarteroni, A.: A patient-specific aor- tic valve model based on moving resistive immersed implicit surfaces. Biomechanics and modeling in mechanobiology **16**, 1779–1803 (2017). https://doi.org/10.1007/s10237-017-0919-1

53. Antiga, L., Steinman, D.: Rethinking turbulence in blood. Biorheology **46**, 77–81 (2009). https://doi.org/10.3233/BIR-2009-0538

54. Nicoud, F., Toda, H., Cabrit, O., Bose, S., Lee, J.: Using singular values to build a subgrid-scale model for large eddy simulation. Physics of Fluids - PHYS FLUIDS **23** (2011). https://doi.org/10.1063/1.3623274

55. Lancellotti, R.M., Vergara, C., Valdettaro, L., Bose, S., Quarteroni, A.: Large eddy simulations for blood dynamics in realistic stenotic carotids. International Journal for Numerical Methods in Biomedical Engineering **33**(11), 2868. https://doi.org/10.1002/cnm.2868

56. Vergara, C., Le Van, D., Quadrio, M., Formaggia, L., Domanin, M.: Large eddy simulations of blood dynamics in abdominal aortic aneurysms. Med- ical Engineering & Physics **47**, 38–46 (2017). https://doi.org/10.1016/j. medengphy.2017.06.030

57. Stella, S., Vergara, C., Giovannacci, L., Quarteroni, A., Prouse, G.: Assessing the disturbed flow and the transition to turbulence in the arte- riovenous fistula. Journal of Biomechanical Engineering **141**(10) (2019). https://doi.org/10.1115/1.4043448

58. Wiggers, C.J.: Modern Aspects of the Circulation in Health and Disease. Journal of the American Medical Association **81**(15), 1305–1305 (1923). https://doi.org/10.1001/jama.1923.02650150059033

59. Mokadam, N., Stout, K., Verrier, E.: Management of acute regurgitation in left-sided cardiac valves. Texas Heart Institute journal / from the Texas Heart Institute of St. Luke's Episcopal Hospital, Texas Children's Hospital **38**, 9–19 (2011)

60. Bertoglio, C., Caiazzo, A., Bazilevs, Y., Braack, M., Esmaily, M., Grave- meier, V., L. Marsden, A., Pironneau, O., E. Vignon-Clementel, I., A. Wall, W.: Benchmark problems

for numerical treatment of back- flow at open boundaries. International Journal for Numerical Methods in Biomedical Engineering **34**(2), 2918 (2018). https://doi.org/10.1002/ cnm.2918

61. Carabello, B.A.: Progress in mitral and aortic regurgitation. Current Problems in Cardiology **28**(10), 553–582 (2003). https://doi.org/10.1016/ j.cpcardiol.2003.10.003

62. Tezduyar, T., Sathe, S.: Stabilization parameters in SUPG and PSPG formulations. Journal of Computational and Applied Mechanics **4**, 71–88 (2003)

63. Forti, D., Ded`e, L.: Semi-implicit BDF time discretization of the Navier–Stokes equations with VMS-LES modeling in a high performance computing framework. Computers & Fluids **117**, 168–182 (2015). https: //doi.org/10.1016/j.compfluid.2015.05.011

64. Africa, P.C., Piersanti, R., Fedele, M., Dede', L., Quarteroni, A.: life^x - heart module: a high-performance simulator for the cardiac function. Package 1: Fiber generation. arXiv (2022). https://doi.org/10.48550/ ARXIV.2201.03303

65. Arndt, D., Bangerth, W., Blais, B., Fehling, M., Gassm¨oller, R., Heister, T., Heltai, L., K¨ocher, U., Kronbichler, M., Maier, M., Munch, P., Pelteret, J.-P., Proell, S., Simon, K., Turcksin, B., Wells, D., Zhang, J.: The deal.ii library, version 9.3. Journal of Numerical Mathematics **29**(3), 171–186 (2021). https://doi.org/10.1515/jnma-2021-0081

66. McCutcheon, K., Manga, P.: Left ventricular remodelling in chronic primary mitral regurgitation: Implications for medical therapy. Cardio- vascular Journal of Africa **29**, 51–65 (2018). https://doi.org/10.5830/ CVJA-2017-009

67. Patel, P., Ambrosy, A., Phelan, M., Alenezi, F., Chiswell, K., Dyke, M., Tomfohr, J., Honarpour, N., Velazquez, E.: Association between systolic ejection time and outcomes in heart failure by ejection fraction. European Journal of Heart Failure **22** (2019). https://doi.org/10.1002/ejhf.1659

68. Gulsin, G.S., Singh, A., McCann, G.P.: Cardiovascular magnetic reso- nance in the evaluation of heart valve disease. BMC Med Imaging **17** (2013). https://doi.org/10.1186/s12880-017-0238-0

69. Carey, R.M., Whelton, P.K.: Prevention, detection, evaluation, and man- agement of high blood pressure in adults: Synopsis of the 2017 American College of Cardiology/American Heart Association Hypertension Guide- line. Annals of Internal Medicine **168**(5), 351–358 (2018). https://doi. org/10.7326/M17-3203

70. Chen, W., Gao, H., Luo, X., Hill, N.: Study of cardiovascular function using a coupled left ventricle and systemic circulation model. Journal of Biomechanics **49** (2016). https://doi.org/10.1016/j.jbiomech.2016.03.009

71. Sun, W., Mao, W., Griffith, B.E.: Chapter 7 - Computer modeling and simulation of heart valve function and intervention. In: Kheradvar, A. (ed.) Principles of Heart Valve Engineering, pp. 177–211 (2019). https: //doi.org/10.1016/B978-0-12-814661-3.00007-1

72. Rusinaru, D., Bohbot, F. Y.and Djelaili, Delpierre, Q., Altes, A., Serbout,S., Kubala, M., Mar´echaux, S., Tribouilloy, C.: Normative reference values of cardiac output by pulsed-wave Doppler echocardiography in adults. The American journal of cardiology **140**, 128–133 (2021). https://doi.org/10. 1016/j.amjcard.2020.10.046

73. Mao, W., Caballero, A., McKay, R., Primiano, C., Sun, W.: Fully-coupled fluid-structure interaction simulation of the aortic and mitral valves in a realistic 3D left ventricle model. PLOS ONE **12**(9), 1–21 (2017). https: //doi.org/10.1371/journal.pone.0184729

74. Vinayagam, D., Patey, O., Thilaganathan, B., Khalil, A., Khalil, D.: Car- diac output assessment in pregnancy: comparison of two automated moni- tors with echocardiography. Ultrasound in Obstetrics and Gynecology **49**, 32–38 (2017). https://doi.org/10.1002/uog.15915

75. Alharthi, M., Mookadam, F., Tajik, J.: Echocardiographic quantitation of mitral regurgitation. Expert review of cardiovascular therapy **6**, 1151–60 (2008). https://doi.org/10.1586/14779072.6.8.1151

76. Pierard, L., Carabello, B.: Ischaemic mitral regurgitation: Pathophysiol- ogy, outcomes and the conundrum of treatment. European heart journal **31**, 2996–3005 (2010). https://doi.org/10.1093/eurheartj/ehq411

77. Salustri, A., Almaghrabi, A.: Mitral valve disease: correlation between the most important echocardiographic parameters and haemodynamics. E-Journal of Cardiology Practice **16** (2018)

78. Carpentier, A.: Cardiac valve surgery-the “French correction”. The Jour- nal of Thoracic and Cardiovascular Surgery **86**(3), 323–337 (1983). https: //doi.org/10.1016/S0022-5223(19)39144-5

79. Stewart, W.J., Currie, P.J., Salcedo, E.E., Klein, A.L., Marwick, T., Agler, D.A., Homa, D., Cosgrove, D.M.: Evaluation of mitral leaflet motion by echocardiography and jet direction by doppler color flow mapping to determine the mechanisms of mitral regurgitation. Journal of the Amer- ican College of Cardiology **20**(6), 1353–1361 (1992). https://doi.org/10. 1016/0735-1097(92)90248-l

80. Filsoufi, F., Carpentier, A.: Principles of reconstructive surgery in degen- erative mitral valve disease. Seminars in thoracic and cardiovascular surgery **19**, 103–10 (2007). https://doi.org/10.1053/j.semtcvs.2007.04. 003

81. Ji, L., Hu, W., Yong, Y., Wu, H., Zhou, L., Xu, D.: Left ventricular energy loss and wall shear stress assessed by vector flow mapping in patients with hypertrophic cardiomyopathy. The International Journal of Cardiovascu- lar Imaging **34** (2018). https://doi.org/10.1007/s10554-018-1348-7

82. Sacco, F., Paun, B., Lehmkuhl, O., Iles, T.L., Iaizzo, P.A., Houzeaux, G., V´azquez, M., Butakoff, C., Aguado-Sierra, J.: Left ventricular trabecu- lations decrease the wall shear stress and increase the intra-ventricular pressure drop in cfd simulations. Frontiers in Physiology **9** (2018). https: //doi.org/10.3389/fphys.2018.00458

83. McCormick, M., Manduchi, E., Witschey, W., Gorman, R., Gorman III, J., Jiang, Y.-Z., Jr, C., Barker, A., Yoon, S., Markl, M., Davies, P.: Spatial phenotyping of the endocardial endothelium as a function of intracardiac hemodynamic shear stress. Journal of Biomechanics 50 (2016). https:// doi.org/10.1016/j.jbiomech.2016.11.018

84. Janse, M.J.: Why does atrial fibrillation occur? European Heart Journal

85. 18, 12–18 (1997). https://doi.org/10.1093/eurheartj/18.suppl C.12

86. Vasan, R.S., Larson, M.G., Levy, D., Evans, J.C., Benjamin, E.J.: Distri- bution and categorization of echocardiographic measurements in relation to reference limits. Circulation 96(6), 1863–1873 (1997).

87. Borger, M.A., Mansour, M.C., Levine, R.A.: Atrial fibrillation and mitral valve prolapse. Journal of the American College of Cardiology 73(3), 275– 277 (2019). https://doi.org/10.1016/j.jacc.2018.11.018

88. Mu¨gge, A., Daniel, W.G., Angermann, C., Spes, C., Khandheria, B.K., Kronzon, I., Freedberg, R.S., Keren, A., Dennig, K., Engberding, R., Sutherland, G.R., Vered, Z., Erbel, R., Visser, C.A., Lindert, O., Haus- mann, D., Wenzlaff, P.: Atrial septal aneurysm in adult patients. Circu- lation 91(11), 2785–2792 (1995). https://doi.org/10.1161/01.CIR.91.11. 2785

89. Dolan, J.M., Kolega, J., Meng, H.: High wall shear stress and spatial gradients in vascular pathology: A review. Ann Biomed Eng 5, 1411–1427 (2013). https://doi.org/10.1007/s10439-012-0695-0

90. Hsu, C.-P.D., Hutcheson, J.D., Ramaswamy, S.: Oscillatory fluid-induced mechanobiology in heart valves with parallels to the vasculature. Vascular Biology 2(1), 59–71 (2020). https://doi.org/10.1530/VB-19-0031

91. Zingaro, A., Fumagalli, I., Dede, L., Fedele, M., Africa, P.C., Corno, A.F., Quarteroni, A.: A geometric multiscale model for the numerical simulation of blood flow in the human left heart. Discrete and Continuous Dynamical Systems - S, (2022). https://doi.org/10.3934/dcdss.2022052

92. Tsao, C.W., Aday, A.W., Almarzooq, Z.I., Alonso, A., Beaton, A.Z., Bittencourt, M.S., Boehme, A.K., Buxton, A.E., Carson, A.P., Commodore-Mensah, Y., Elkind, M.S.V., Evenson, K.R., Eze-Nliam, C., Ferguson, J.F., Generoso, G., Ho, J.E., Kalani, R., Khan, S.S., Kissela, B.M., Knutson, K.L., Levine, D.A., Lewis, T.T., Liu, J., Loop, M.S., Ma, J., Mussolino, M.E., Navaneethan, S.D., Perak, A.M., Poudel, R., Rezk-Hanna, M., Roth, G.A., Schroeder, E.B., Shah,a. H., Thacker, E.L., VanWagner, L.B., Virani, S.S., Voecks, J.H., Wang, N.-Y., Yaffe, K., Martin, S.S.: Heart disease and stroke statistics2022 update: A report from the American Heart Association. Circulation 145(8), 153–639

93. Dyverfeldt, P., Kvitting, J.-P.E., Carlhäll, C.J., Boano, G., Sigfridsson, A., Hermansson, U., Bolger, A.F., Engvall, J., Ebbers, T.: Hemodynamic aspects of mitral regurgitation assessed by generalized phase-contrast mri. Journal of Magnetic Resonance Imaging 33(3), 582–588 (2011). https://doi.org/10.1002/jmri.2240

94. Sugiura, T., Okumiya, T., Kamioka, M., Kubo, T., Hirakawa, Y., Hisahara, T., Matsumura, Y.: Intravascular hemolysis in patients with mitral regurgitation: Evaluation by erythrocyte creatine. Journal of Cardiology 71(4), 414–418 (2018). https://doi.org/10.1016/j.jjcc.2017.10.006. Topics in mitral valve repair

95. Cresti, A., Galli, C.A., Alimento, M.L., De Sensi, F., Baratta, P., D'Aiello, I., Limbruno, U., Pepi, M., Fusini, L., Malt-agliati, A.C.: Does mitral regurgitation reduce the risks of thrombosis in atrial fibrillation and flutter? Journal of Cardio-vascular Medicine 20(10) (2019). https://doi.org/10.2459/JCM.0000000000000838

96. Kon, M., Myerson, S., Moat, N., Pennell, D.: Quantification of regurgitant fraction in mitral regurgitation by cardiovas-cular magnetic resonance: Comparison of techniques. The Journal of heart valve disease 13, 600–7 (2004)

97. Myerson, S.G., dArcy, J., Christiansen, J.P., Dobson, L.E., Mohiaddin, R., Francis, J.M., Prendergast, B., Green-wood, J.P., Karamitsos, T.D., Neubauer, S.: Determination of clinical outcome in mitral regurgitation with cardiovas-cular Magnetic Resonance quantification. Circulation 133(23), 2287–2296 (2016). https://doi.org/10.1161/CIRCULATIONAHA.115.017888

98. Ngo, M.T., Kim, C.I., Jung, J., Chung, G.H., Lee, D.H., Kwak, H.S.: Four-dimensional flow magnetic resonance imag-ing for assessment of velocity magnitudes and flow patterns in the human carotid artery bifurcation: Comparison with computational fluid dynamics. Diagnostics 9(4) (2019). https://doi.org/10.3390/diagnostics9040223

99. Augst, A.D., Ariff, B., McG. Thom, S.A.G., Xu, X.Y., Hughes, A.D.: Analysis of complex flow and the relation-ship between blood pressure, wall shear stress, and intima-media thickness in the human carotid artery. American Journal of Physiology-Heart and

Circulatory Physiology 293(2), 1031–1037 (2007). https://doi.org/10.1152/ajpheart.00989.2006

100. Groen, H.C., Gijsen, F.J.H., van der Lugt, A., Ferguson, M.S., Hatsukami, T.S., van der Steen, A.F.W., Yuan, C., Wentzel, J.: Plaque rupture in the carotid artery is localized at the high shear stress region. Stroke 38(8), 2379–2381 (2007).

101. Bazilevs, Y., Hsu, M.-C., Benson, D.J., Sankaran, S., Marsden, A.L.: Computational fluid–structure interaction: methods and application to a total cavopulmonary connection. Computational Mechanics 45(1), 77–89 (2009). https://doi. org/10.1007/s00466-009-0419-y

102. Esmaily, M., Kahn, A., Tseng, E., Guccione, J., Marsden, A.: Patient-specific multiscale modeling of blood flow for coronary artery bypass graft surgery. Annals of biomedical engineering 40, 2228–42 (2012). https://doi.org/10. 1007/s10439-012-0579-3

103. Schrauwen, J.T.C., Schwarz, J.C.V., Wentzel, J.J., van der Steen, A.F.W., Siebes, M., Gijsen, F.J.H.: The impact of scaled boundary conditions on wall shear stress computations in atherosclerotic human coronary bifurcations. American Journal of Physiology-Heart and Circulatory Physiology 310(10), 1304–1312 (2016). https://doi.org/10.1152/ajpheart.00896.2015

104. Liu, X., Zhang, H., Ren, L., Xiong, H., Gao, Z., Xu, P., Huang, W., Wu, W.: Functional assessment of the stenotic carotid artery by cfd-based pressure gradient evaluation. American Journal of Physiology-Heart and Circulatory Physiol-ogy 311(3), 645–653 (2016). https://doi.org/10.1152/ajpheart.00888.2015

105. Colebank, M.J., Qureshi, M.U., Rajagopal, S., Krasuski, R.A., Olufsen, M.S.: A multiscale model of vascular function in chronic thromboembolic pulmonary hypertension. American Journal of Physiology-Heart and Circulatory Physiology 321(2), 318–338 (2021). https://doi.org/10.1152/ajpheart.00086.2021

106. Ma, X., Gao, H., Griffith, B.E., Berry, C., Luo, X.: Image-based fluidstructure interaction model of the human mitral valve. Computers & Fluids 71, 417–425 (2013). https://doi.org/10.1016/j.compfluid.2012.10.025

107. Caballero, A., Mao, W., McKay, R., Primiano, C., Hashim, S., Sun, W.: New insights into mitral heart valve prolapse after chordae rupture through fluidstructure interaction computational modeling. Scientific Reports 8 (2018). https: //doi.org/10.1038/s41598-018-35555-5

108. Fuchsberger, J., Karabelas, E., Aigner, P., Schima, H., Haase, G., Plank, G.: Validation study of computational fluid dynamics models of hemodynamics in the human aorta. PAMM 19(1), 201900472 (2019). https://doi.org/10. 1002/pamm.201900472

109. Feng, L., Gao, H., Griffith, B., Niederer, S., Luo, X.: Analysis of a coupled fluid-structure interaction model of the left atrium and mitral valve. International Journal for Numerical Methods in Biomedical Engineering 35(11), 3254 (2019). https://doi.org/10.1002/cnm.325

110. Karabelas, E., Longobardi, S., Fuchsberger, J., Razeghi, O., Rodero, C., Strocchi, M., Rajani, R., Haase, G., Plank, G., Niederer, S.: Global sensitivity analysis of four chamber heart hemodynamics using surrogate models. IEEE Transactions on Biomedical Engineering 69(10), 3216–3223 (2022). https://doi.org/10.1109/TBME.2022.3163428

111. Meschini, V., Viola, F., Verzicco, R.: Modeling mitral valve stenosis: A parametric study on the stenosis severity level. Journal of Biomechanics 84, 218–226 (2019). https://doi.org/10.1016/j.jbiomech.2019.01.002

112. Meschini, V., Mittal, R., Verzicco, R.: Systolic anterior motion in hypertrophic cardiomyopathy: a fluid–structure interaction computational model. Theoretical and Computational Fluid Dynamics 35(3), 381–396 (2021). https: //doi.org/10.1007/s00162-021-00564-

113. Spühler, J.H., Jansson, J., Jansson, N., Hoffman, J.: 3d fluid-structure interaction simulation of aortic valves using a unified continuum ale fem model. Frontiers in Physiology 9 (2018). https://doi.org/10.3389/fphys.2018. 00363

114. Luraghi, G., Migliavacca, F., García, A., Chiastra, C., Rossi, A., Cao, D., Stefanini, G., Rodriguez, J.: On the modeling of patient-specific transcatheter aortic valve replacement: A fluid-structure interaction approach. Cardiovascular Engineering and Technology 10, 1–19 (2019). https://doi.org/10.1007/s13239-019-00427-0

115. Caballero, A., Mao, W., McKay, R., Sun, W.: Transapical mitral valve repair with neochordae implantation: FSI analysis of neochordae number and complexity of leaflet prolapse. International Journal for Numerical Methods in Biomedical Engineering 36(3), 3297 (2020). https://doi.org/10.1002/cnm.3297

116. Seo, J.H., Vedula, V., Abraham, T., Lardo, A., Dawoud, F., Luo, H., Mittal, R.: Effect of the mitral valve on diastolic flow patterns. Physics of Fluids 26, 121901 (2014). https://doi.org/10.1063/1.4904094

117. Su, B., Tan, R.S., Tan, J.L., Guo, K.W.Q., Zhang, J.M., Leng, S., Zhao, X., Allen, J.C., Zhong, L.: Cardiac MRI based numerical modeling of left ventricular fluid dynamics with mitral valve incorporated. Journal of Biomechanics 49(7), 1199–1205 (2016). https://doi.org/10.1016/j.jbiomech.2016.03.008

118. Chnafa, C., Mendez, S., Franck, N.: Image-based large-eddy simulation in a realistic left heart. Computers & Fluids 94, 173–187 (2014). https://doi.org/10.1016/j.compfluid.2014.01.030

119. Bavo, A., Pouch, A., Degroote, J., Vierendeels, J., Gorman III, J., Gorman, R., Segers, P.: Patient-specific CFD simulation of intraventricular haemodynamics based on 3D ultrasound imaging. Biomedical engineering online 15 (2016). https: //doi.org/10.1186/s12938-016-0231-9

120. Bavo, A., Pouch, A., Degroote, J., Vierendeels, J., Gorman III, J., Gorman, R., Segers, P.: Patient-specific CFD models for intraventricular flow analysis from 3D ultrasound imaging: Comparison of three clinical cases. Journal of Biomechanics 50 (2016). https://doi.org/10.1016/j.jbiomech.2016.11.039

121. Chnafa, C., Mendez, S., Nicoud, F.: Image-based simulations show important flow fluctuations in a normal left ventricle: What could be the implications? Annals of Biomedical Engineering 44(11), 3346–3358 (2016). https://doi.org/ 10.1007/s10439-016-1614-6

122. Fumagalli, I., Fedele, M., Vergara, C., Dede, L., Ippolito, S., Nicolò, F., Antona, C., Scrofani, R., Quarteroni, A.: An image-based computational hemodynamics study of the systolic anterior motion of the mitral valve. Computers in Biology and Medicine 123, 103922 (2020). https://doi.org/10.1016/j.compbiomed.2020.103922

123. Fumagalli, I., Vitullo, P., Vergara, C., Fedele, M., Corno, A.F., Ippolito, S., Scrofani, R., Quarteroni, A.: Image-based computational hemodynamics analysis of systolic obstruction in hypertrophic cardiomyopathy. Frontiers in Physiology 12 (2022). https://doi.org/10.3389/fphys.2021.78708

124. Collia, D., Zovatto, L., Pedrizzetti, G.: Analysis of mitral valve regurgitation by computational fluid dynamics. APL Bioengineering 3(3), 036105 (2019). https://doi.org/10.1063/1.509724

125. Obermeier, L., Vellguth, K., Schlief, A., Tautz, L., Brüning, J., Knosalla, C., Kuehne, T., Solowjowa, N., Goubergrits, L.: CT-based simulation of left ventricular hemodynamics: A pilot study in mitral regurgitation and left ventricle aneurysm patients. Frontiers in Cardiovascular Medicine 9, 828556 (2022). https://doi.org/10.3389/fcvm. 2022.828556

126. Bennati, L., Vergara, C., Giambruno, V., Fumagalli, I., Corno, A.F., Quarteroni, A., Puppini, G., Luciani, G.B.: An image-based computational fluid dynamics study of mitral regurgitation in presence of prolapse. Cardiovascular Engineering and Technology, to appear (2023)

127. Du Bois, D., Du Bois, E.F.: A formula to estimate the approximate surface area if height and weight be known. 1916. Nutrition 5(5), 303–11 (1989)

128. Renzi, F., Vergara, C., Fedele, M., Giambruno, V., Puppini, G., Quarteroni, A., Luciani, G.B.: Cine-MRI multi-image based reconstruction of the right heart in view of computational fluid dynamics. In preparation (2022)

129. Stevanella, M., Maffessanti, F., Conti, C., Votta, E., Arnoldi, A., Lombardi, M., Parodi, O., Caiani, E., Redaelli, A.: Mitral valve patient-specific finite element modeling from cardiac mri: Application to an annuloplasty procedure. Cardiovascular Engineering and Technology 2, 66–76 (2011). https://doi.org/10.1007/s13239-010-0032-4

130. Fetzer, A., Zelzer, S., Schroeder, T., Meinzer, H.-P., Nolden, M.: An interactive 3D segmentation for the Medical Imaging Interaction Toolkit (MITK). (2014). https://doi.org/10.13140/2.1.4169.6326

131. Antiga, L., Piccinelli, M., Botti, L., Ene-Iordache, B., Remuzzi, A., Steinman, D.A.: An image-based modeling frame-work for patient-specific computational hemodynamics. Medical & biological engineering & computing 46(11), 1097–1112 (2008). https://doi.org/10.1007/s11517-008-0420-1

132. Fedele, M., Quarteroni, A.: Polygonal surface processing and mesh generation tools for the numerical simulation of the cardiac function. International Journal for Numerical Methods in Biomedical Engineering 37 (2021). https://doi. org/10.1002/cnm.3435

133. Klein, S., Staring, M., Murphy, K., Viergever, M.A., Pluim, J.P.W.: Elastix: A toolbox for intensity-based medical image registration. IEEE Transactions on Medical Imaging 29(1), 196–205 (2010). https://doi.org/10.1109/TMI. 2009.2035616

134. Gaidulis, G., Selmi, M., Zakarkaite, D., Aidietis, A., Kaianauskas, R.: Modelling and simulation of mitral valve for transapical repair applications. Nonlinear Analysis: Modelling and Control 24, 485–502 (2019). https://doi.org/ 10.15388/NA.2019.4.

135. Quarteroni, A., Sacco, R., Saleri, F.: Numerical Mathematics vol. 37. Springer, ??? (2007). https://doi.org/10. 1007/b98885

136. Quarteroni, A.: Numerical Models for Differential Problems vol. 2. Springer, ??? (2013). https://doi.org/10. 1007/978-88-470-1071-

137. Donea, J., Giuliani, S., Halleux, J.P.: An arbitrary Lagrangian-Eulerian finite element method for transient dynamic fluid-structure interactions. Computer Methods in Applied Mechanics and Engineering 33(1), 689–723 (1982). https: //doi.org/10.1016/0045-7825(82)90128-1

138. Fernández, Miguel A., Gerbeau,Jean-Frédéric, Martin, Vincent: Numerical simulation of blood flowsthrough a porous interface. ESAIM: M2AN 42(6), 961–990 (2008). https://doi.org/10.1051/m2an:200803

139. Fedele, M., Faggiano, E., Dede, L., Quarteroni, A.: A patient-specific aortic valve model based on moving resistive immersed implicit surfaces. Biomechanics and modeling in mechanobiology 16, 1779–1803 (2017). https://doi. org/10.1007/s10237-017-0919-

140. Nicoud, F., Toda, H., Cabrit, O., Bose, S., Lee, J.: Using singular values to build a subgrid-scale model for large eddy simulation. Physics of Fluids - PHYS FLUIDS 23 (2011). https://doi.org/10.1063/1.3623274

141. Vergara, C., Le Van, D., Quadrio, M., Formaggia, L., Domanin, M.: Large eddy simulations of blood dynamics in abdominal aortic aneurysms. Medical Engineering & Physics 47, 38–46 (2017). https://doi.org/10.1016/j. medengphy.2017.06.030

142. Stella, S., Vergara, C., Giovannacci, L., Quarteroni, A., Prouse, G.: Assessing the disturbed flow and the transition to turbulence in the arteriovenous fistula. Journal of Biomechanical Engineering 141(10) (2019). https://doi.org/ 10.1115/1.404344

143. Stein, K., Tezduyar, T., Benney, R.: Mesh moving techniques for fluid-structure interactions with large displacements. Journal of Applied Mechanics 70(1), 58–63 (2003). https://doi.org/10.1115/1.1530635

144. Bucelli, M., Zingaro, A., Africa, P.C., Fumagalli, I., Dede', L., Quarteroni, A.: A mathematical model that integrates cardiac electrophysiology, mechanics, and fluid dynamics: Application to the human left heart. International Journal for Numerical Methods in Biomedical Engineering, 3678 (2023). https://doi.org/10.1002/cnm.367

145. Quarteroni, A., Manzoni, A., Vergara, C.: The cardiovascular system:˘amathematical modelling, numerical algorithms and clinical applications. Acta Numerica 26, 365–590 (2017). https://doi.org/10.1017/S0962492917000046

146. Wiggers, C.J.: Modern Aspects of the Circulation in Health and Disease. Journal of the American Medical Association 81(15), 1305–1305 (1923). https://doi.org/10.1001/jama.1923.0265015005903

147. Brath, P.C., Eisenach, J.: Atlas of Cardiovascular Monitoring. Anesthesiology 93(1), 312–312 (2000). https://doi. org/10.1097/00000542-200007000-0006

148. Bertoglio, C., Caiazzo, A., Bazilevs, Y., Braack, M., Esmaily, M., Gravemeier, V., Marsden, A., Pironneau, O., Vignon-Clementel, I., Wall, W.: Benchmark problems for numerical treatment of backflow at open boundaries. International Journal for Numerical Methods in Biomedical Engineering 34(2), 2918 (2018). https://doi.org/10.1002/cnm. 2918

149. Tezduyar, T., Sathe, S.: Stabilization parameters in SUPG and PSPG formulations. Journal of Computational and Applied Mechanics 4, 71–88 (2003)

150. Africa, P.: li f ex: A flexible, high performance library for the numerical solution of complex finite element problems. SoftwareX 20, 101252 (2022). https://doi.org/10.1016/j.softx.2022.101252

151. Arndt, D., Bangerth, W., Blais, B., Fehling, M., Gassmöller, R., Heister, T., Heltai, L., Köcher, U., Kronbichler, M., Maier, M., Munch, P., Pelteret, J.-P., Proell, S., Simon, K., Turcksin, B., Wells, D., Zhang, J.: The deal.II library, version 9.3. Journal of Numerical Mathematics 29(3), 171–186 (2021). https://doi.org/10.1515/jnma-2021-0081

152. Katritsis, D., Kaiktsis, L., Chaniotis, A., Pantos, J., Efstathopoulos, E.P., Marmarelis, V.: Wall shear stress: Theoretical considerations and methods of measurement. Progress in Cardiovascular Diseases 49(5), 307–329 (2007). https://doi.org/10.1016/j.pcad.2006.11.001. Special Articles

153. Janse, M.J.: Why does atrial fibrillation occur? European Heart Journal 18, 12–18 (1997). https://doi.org/10. 1093/eurheartj/18.suppl_C.1

154. Riccardello, G.J., Shastri, D.N., Changa, A.R., Thomas, K.G., Roman, M., Prestigiacomo, C.J., Gandhi, C.D.: Influence of relative residence time on side-wall aneurysm inception. Neurosurgery 83(3) (2018)

155. Harfi, T.T., Seo, J.-h., Yasir, H.S., Welsh, N., Mayer, S.A., Abraham, T.P., George, R.T., Mittal, R.: The e-wave prop-agation index (epi): A novel echocardiographic parameter for prediction of left ventricular thrombus. derivation from computational fluid dynamic modeling and validation on human subjects. International Journal of Cardiology 227, 662–667 (2017). https://doi.org/10.1016/j.ijcard.2016.10.079

156. Baldwin, J.T., Deutsch, S., Petrie, H.L., Tarbell, J.M.: Determination of Principal Reynolds Stresses in Pulsatile Flows After Elliptical Filtering of Discrete Velocity Measurements. Journal of Biomechanical Engineering 115(4A), 396–403 (1993). https://doi.org/10.1115/1.2895503

157. Lu, P.C., Lai, H.C., Liu, J.S.: A reevaluation and discussion on the threshold limit for hemolysis in a turbulent shear flow. Journal of Biomechanics 34(10), 1361–1364 (2001). https://doi.org/10.1016/S0021-9290(01)00084-7

158. Gaasch, W.H., Meyer, T.E.: Left ventricular response to mitral regurgitation. Circulation 118(22), 2298–2303 (2008). https://doi.org/10.1161/CIRCULATIONAHA.107.755942

159. Mokadam, N., Stout, K., Verrier, E.: Management of acute regurgitation in left-sided cardiac valves. Texas Heart Institute journal / from the Texas Heart Institute of St. Luke's Episcopal Hospital, Texas Children's Hospital 38, 9–19 (2011)

160. Schiller, N.B., Foster, E., Redberg, R.F.: Transesophageal echocardiography in the evaluation of mitral regurgitation: The twenty-four signs of severe mitral regurgitation. Cardiology Clinics 11(3), 399–408 (1993). https://doi.org/10. 1016/S0733-8651(18)30157-7. Transesophageal Echocardiography

161. Yaghi, S., Song, C., Gray, W.A., Furie, K.L., Elkind, M.S.V., Kamel, H.: Left atrial appendage function and stroke risk. Stroke 46(12), 3554–3559 (2015). https://doi.org/10.1161/STROKEAHA.115.011273

162. Kalaria, V.G., Passannante, M.R., Shah, T., Modi, K., Weisse, A.B.: Effect of mitral regurgitation on left ventricular thrombus formation in dilated cardiomyopathy. American Heart Journal 135(2), 215–220 (1998). https://doi.org/ 10.1016/S0002-8703(98)70084-5

163. Van Laer, S.L., Verreyen, S., Winkler, K.M., Miljoen, H., Sarkozy, A., Heuten, H., Saenen, J., Van Herck, P., Van de Heyn-ing, C.M., Heidbuchel, H., Claeys, M.J.: Effect of mitral regurgitation on thrombotic risk in patients with nonrheumatic atrial fibrillation: A new cha2ds2-vasc score risk modifier? The American Journal of Cardiology 145, 69–76 (2021). https://doi.org/10.1016/j.amjcard.2021.01.006

164. Delahaye, J.P., Gare, J.P., Viguier, E., Delahaye, F., De Gevigney, G., Milon, H.: Natural history of severe mitral regurgi-tation. European Heart Journal 12, 5–9 (1991). https://doi.org/10.1093/eurheartj/12.suppl_B.

165. Tribouilloy, C., Grigioni, F., Avierinos, J.F., Barbieri, A., Rusinaru, D., Szymanski, C., Ferlito, M., Tafanelli, L., Bursi, F., Trojette, F., Branzi, A., Habib, G., Modena, M.G., Enriquez-Sarano, M.: Survival implication of left ventricular end-systolic diameter in mitral regurgitation due to flail leaflets: A long-term follow-up multicenter study. Journal of the American College of Cardiology 54(21), 1961–1968 (2009). https://doi.org/10.1016/j.jacc.2009.06. 04

166. Narayanan, K., Reinier, K., Rusinaru, C., Evanado, A., Aleong, R., Chugh, H., Nichols, G., Gunson, K., London, B., Jui, J., Chugh, S.: Left ventricular diameter and risk stratification for sudden cardiac death. Journal of the American Heart Association 3 (2014). https://doi.org/10.1161/JAHA.114.001193

167. Yeo, T.C., Freeman, W.K., Schaff, H.V., Orszulak, T.A.: Mechanisms of hemolysis after mitral valve repair: assessment by serial echocardiography. Journal of the American College of Cardiology 32(3), 717–723 (1998). https://doi. org/10.1016/S0735-1097(98)00294-0

168. Carpentier, A.: Cardiac valve surgerythe french correction. The Journal of Thoracic and Cardiovascular Surgery 86(3), 323–337 (1983). https://doi.org/10.1016/S0022-5223(19)39144-5

169. Stewart, W.J., Currie, P.J., Salcedo, E.E., Klein, A.L., Marwick, T., Agler, D.A., Homa, D., Cosgrove, D.M.: Evaluation of mitral leaflet motion by echocardiography and jet direction by doppler color flow mapping to determine the mechanism of mitral regurgitation. Journal of the American College of Cardiology 20(6), 1353–1361 (1992). https://doi.org/10.1016/0735-1097(92)90248-L

170. Firstenberg, M.S., Vandervoort, P.M., Greenberg, N.L., Smedira, N.G., McCarthy, P.M., Garcia, M.J., Thomas, J.D.: Noninvasive estimation of transmitral pressure drop across the normal mitral valve in humans: importance of convective and inertial forces during left ventricular filling. Journal of the American College of Cardiology 36(6), 1942–1949 (2000)

171. Thomas, L., Foster, E., Schiller, N.B.: Peak mitral inflow velocity predicts mitral regurgitation severity. Journal of the American College of Cardiology 31(1), 174–179 (1998). https://doi.org/10.1016/S0735-1097(97) 00454-3

172. Broomé, M., Maksuti, E., Bjällmark, A., Frenckner, B., Janerot-Sjöberg, B.: Closed-loop real-time simulation model of hemodynamics and oxygen transport in the cardiovascular system. Biomedical engineering online 12, 69 (2013). https: //doi.org/10.1186/1475-925X-12-69

173. Yoganathan, A.P., He, Z., Casey Jones, S.: Fluid mechanics of heart valves. Annual Review of Biomedical Engi-neering 6(1), 331–362 (2004). https://doi.org/10.1146/annurev.bioeng.6.040803.140111. PMID: 15255773